Scientific Research Publishing

Open Journal of Geology, 2025, 15(8), 455-491
https://www.scirp.org/journal/ojg
ISSN Online: 2161-7589
ISSN Print: 2161-7570

Granitoid Fertility Assessment as a Potential Source Rock for Granite-Related Hydrothermal Uranium Mineralisation in the Kindi Radiometric Anomalous Area, Central West Region, Burkina Faso (West Africa)

Paul Ismaël Ouedraogo[1,2], Urbain Wenmenga[1], Wendkouni Passecdé Pauline Zongo[1,3], Ignace Dabone[1,2], Christophe Bonnetti[4], Gounwendmanaghré Hubert Zongo[5]

[1]Laboratoire Géosciences et Environnement (LaGE), Département des Sciences de la Terre, Université Joseph Ki-Zerbo, Ouagadougou, Burkina Faso
[2]Bureau des Mines et de la Géologie du Burkina (BUMIGEB), Ouagadougou, Burkina Faso
[3]Unité de Formation et de Recherche en Sciences et Technologies (UFR-ST), Université Lédéa Bernard Ouedraogo, Ouahigouya, Burkina Faso
[4]Arethuse Geology EURL, Fuveau, France
[5]Ecole Supérieure d'Ingénieries, Université Yembila Abdoulaye Toguyeni, Fada N'gourma, Burkina Faso
Email: oued_amsix@yahoo.fr

How to cite this paper: Ouedraogo, P.I., Wenmenga, U., Zongo, W.P.P., Dabone, I., Bonnetti, C. and Zongo, G.H. (2025) Granitoid Fertility Assessment as a Potential Source Rock for Granite-Related Hydrothermal Uranium Mineralisation in the Kindi Radiometric Anomalous Area, Central West Region, Burkina Faso (West Africa). *Open Journal of Geology*, **15**, 455-491.
https://doi.org/10.4236/ojg.2025.158022

Received: May 22, 2025
Accepted: August 19, 2025
Published: August 22, 2025

Abstract

National-scale uranium resource potential assessment in Burkina Faso revealed several radiometric anomalies detected by airborne spectrometric geophysical surveys. These anomalies (>8 ppm eU) are mainly associated with granitoids, which account for around 50% of the country's geological framework. The Koudougou anomalous zone in central-western Burkina Faso accounts for one of the most significant radiometric anomalies, mainly associated with syn- to late- and post-orogenic granitoids of the Kindi area, including medium-grained biotite granite, porphyroid biotite granite, and two-mica leucogranite, along with aplo-pegmatite veins, which are intruded into early granodiorite/trondhjemite and tonalite from the pre-orogenic domain. The pre-orogenic granitoids, defined as poorly fractionated, low-K, calc-alkaline, biotite- and amphibole-bearing facies rich in Na (4.41 - 5.10 wt% oxide), Ca (3.04 - 3.87 wt% oxide), Fe (2.9 - 4.18 wt% oxide), and Mg (1.52 - 2.19 wt% oxide) but with relatively low U and Th concentrations, are defined as non-favourable sources for a granite-related hydrothermal uranium system. In contrast, the syn- to late- and post-orogenic granitoids are characterised by fractionated high-K calc-alkaline to shoshonitic magmatic series with a biotite,

sphene, allanite, and (+/− muscovite) mineral assemblage. They display low Na (3.52 - 4.64 wt% oxide), Ca (0.92 - 2.23 wt% oxide), Fe (0.85 - 2.90 wt% oxide), and Mg (0.08 - 1.11 wt% oxide) contents but are relatively enriched in incompatible elements such as U (2.8 - 10.9 ppm) and Th (7.50 - 24 ppm), which could be explained by crustal reworking during partial melting of the source magmas. The metamict textures observed around allanite and sphene crystals of these granitoids suggest that these accessory minerals are likely the major host of uranium, which may have been released from the mineral structure and then leached during late magmatic to later hydrothermal alteration and mobilised along the structures, as demonstrated by Th/U > 10 (*i.e.*, U leaching) or Th/U ≤ 1 (U enrichment) in some samples. Therefore, this type of U-rich granite may represent a fertile U source for potential granite-related hydrothermal mineralisation in the region, as a similar typology of late Birrimian granitoids in other parts of the West African Craton (Senegal and Mauritania) have already demonstrated their potential in sourcing hydrothermal uranium mineralisation.

Keywords

Uranium Sources, Radiometric Anomaly, Orogenic Arc Granitoid, Hydrothermal Alteration, Kindi

1. Introduction

Regional-scale prospectivity evaluation for the potential discovery of economic uranium mineralization in Burkina Faso identified several radiometrically anomalous areas, detected by airborne spectrometric geophysical surveys. The most prominent of these anomalies were followed up with ground radiometric verifications and systematic descriptions of outcrop conditions, along with rock sampling for geochemical and petrographic characterization. The first major uranium anomaly in Burkina Faso was identified in the basal sandstones of the Volta Basin near the village of Kodjiari in the East Region [1]. Other significant radiometric anomalies are associated with pegmatites in the Northwest (Ouro) and in the Southwest (Mangodara) of the country, whereas more sporadic radiometric peaks have also been identified in the Northeast. The contact zone between the sandstone formations and the crystalline basement in the Bobo-Dioulasso area to beyond Sindou in the western part of Burkina Faso also exhibits a series of radiometric anomalies [2]. Previous investigations, including a regional survey and reinterpretation of airborne spectrometric geophysical data covering three-quarters of the country, led to the delineation of 33 anomalous zones, among which the Kindi area appeared as one of the most suitable for the implementation of detailed work to evaluate its potential for uranium mineralization [3]. An additional series of 12 highly favorable anomalies was also identified in the northeastern quarter of the country [4]. A geological analysis centered on these identified anomalous

zones revealed that most of the radiometric anomalies are associated with Paleoproterozoic basement, specifically intrusive or anatectic granitoids. Overall, scientific investigations on these Paleoproterozoic granitoids in Burkina Faso have been directed toward geological mapping at various scales [5]-[7], their typology [8] [9], and the geodynamic context of their emplacement [10]-[13]. Except for metallogenic studies conducted on the fertility of plutonic intrusions related to Cu-Au porphyry deposits [14] and research on rare metal resource potential [15] [16], the uranium enrichment of Paleoproterozoic granitic rocks and its potential to source granite-related hydrothermal mineralization has not been addressed. However, performing exploration targeting of most uranium deposits at the regional scale following the mineral system approach [17] inevitably involves assessing the potential of igneous rocks to serve as effective sources of economic uranium concentrations within a given metallogenic province [18]. For instance, several other regions of the West African Craton (WAC) have demonstrated the key role of Paleoproterozoic granitoids in providing significant uranium resources to mineral systems, such as surficial calcrete deposits derived from the weathering of these granites in the Reguibat Shield, Mauritania [19], or magmatic-hydrothermal mineralization that originated from enriched granitic melts of the Saraya Batholith, Senegal [20]. In Burkina Faso, the Koudougou area hosts the highest number of radiometric anomalies that were identified through an airborne radiometric survey (**Figure 1(a)** and **Figure 1(b)**)—the most prominent of those being associated with the Kindi granitoids (**Figure 1(c)**). Therefore, we propose a detailed petrographic and geochemical characterization of the Kindi granitoids to further assess the uranium fertility of these granitoids and their potential role as a primary source to form economic, granite-related hydrothermal uranium mineralization within this region.

2. Geological Setting of the Study Area

The Kindi radiometric anomalous area is located approximately 60 km west of Ouagadougou, between 12˚ and 13˚ North and 1˚ and 3˚ West geographic coordinates (**Figure 1(a)**). This area belongs to the Centre-Ouest region, within the delimited square degree of Koudougou, which contains nine radiometric anomalies associated with Paleoproterozoic granitoids, including Youlou, Bagueou, Guigui, and Boromo 1 and 2 located to the southwest of the Perkoa mine, and Bongo, Villy, and Kindi to the east-northeast of Perkoa (**Figure 1(b)**).

The topography of the area consists of a peneplain with average altitudes ranging between 200 m and 300 m. It includes lateritic plateaus, which are more or less dismantled, as well as sparse sandy alluvial deposits around seasonal backwaters and watercourses. The highest elevations are located upstream of lateritic glacis and on granitic inselbergs, which are associated with block fields and tors.

The Kindi anomaly, like the other neighboring anomalies, belongs to the Paleoproterozoic Baoulé-Mossi domain of the WAC (**Figure 1(a)**). Radiometric anomalies of this area are part of the Koudougou-Tumu Metamorphic and Anatectic Complex (MAC), as defined by [6]. The main lithologies of this complex, as

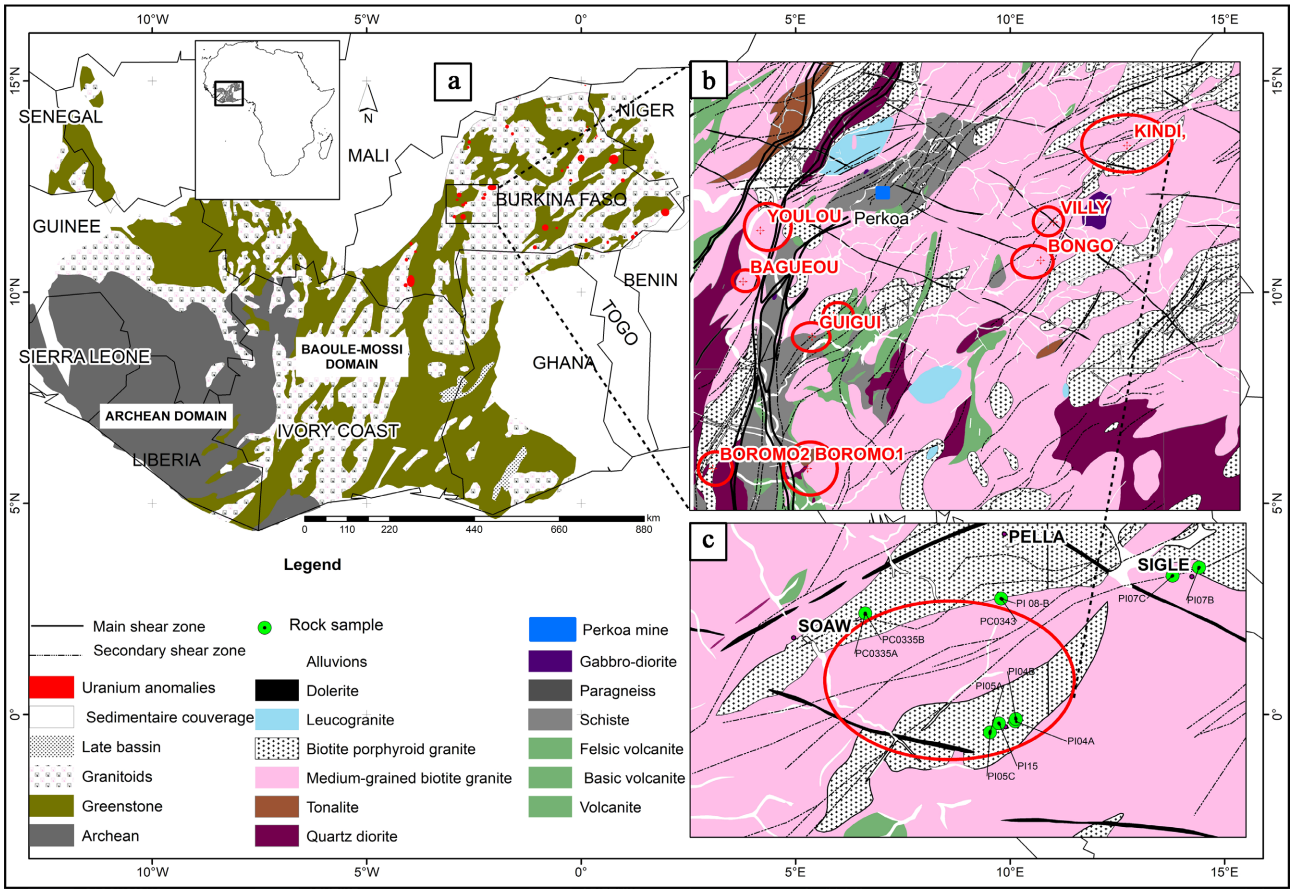

Figure 1. Regional geological context of the radiometric U-Th-K anomaly of Kindi and neighboring anomalous target areas: (a) Simplified geological map of the southern WAC (Leo-Man Shield); (b) Extract from the geological map of the Koudougou sheet [21] displaying the nine radiometric anomalous areas identified from the geophysical survey. The size of the radiometric anomalies on the map of (a) is proportional to the spatial extent of the anomaly defined for values of Uequivalent > 8 ppm and U/Th < 1 [3]. (c) Extract from the geological map of the Koudougou sheet showing the geological setting of the Kindi anomalous area.

described in [21], are comprised of granodiorite and tonalite, associated with gabbro-diorite, which contains lenses of amphibolitized basalt and/or amphibolite (**Figure 1(b)**). These variably metamorphosed mafic to intermediate igneous rocks are intruded by medium-grained biotite granite, dated between 2143 ± 4 Ma and 2150 Ma, as well as porphyroid biotite granite dated at 2110 ± 8 Ma. These rocks are affected by secondary structures of the main translithospheric N-S-trending Wa-Laura-Jirapa shear corridor [6], which affects the rocks of the central part of the Boromo Volcano-Sedimentary Belt (VSB) and the edge of the Koudougou-Tumu MAC and which extends from Ghana to the Mali border, following a strike-slip sinistral movement. The lithologies of these zones are intruded by a late swarm of dolerite dykes that are oriented NW-SE and NE-SW.

3. Methodology

Our approach consisted of 1) a geological and metallogenic synthesis based on available scientific literature and technical historical reports, 2) the processing of

U-Th-K spectrometric data acquired through a regional airborne geophysical survey [3] and ranking of identified radiometric anomalies to define strategic exploration targets, and 3) follow-up field verifications, mapping, and description of key outcrops related to the identified anomalies, as well as systematic rock sampling of suitable lithologies to conduct whole-rock geochemical analysis.

The fieldwork enabled us to refine the geological mapping of the different lithologies within and around the Kindi radiometric anomaly. The systematic and representative sampling of granitoid outcrops allowed for the preparation of 15 thin sections and polished sections by the "Magmas et Volcans" (LVM) laboratory at the Université Clermont Auvergne (France). These thin sections were subjected to petrographic and mineralogical characterization through optical microscopy. The chemical composition of certain minerals (feldspar, biotite, carbonates, oxides, and sphene) from the granitoids was quantified using electron microprobe analysis (EMPA) with the CAMECA SX100 apparatus from the LVM laboratory. Whole-rock geochemical analysis was conducted on 13 samples for the quantification of major and trace elements (including rare earth elements and uranium) by inductively coupled plasma-atomic energy absorption, with mass spectrometry (ICP-AES/MS), in the LMV laboratory (France)—samples PI04A, PI04B, PI05A, PI05C, PI07B, PI07C, and PI15—and Acmelabs (Canada)—samples PC0334, PC0335A, PC0335B, PC0343, PC0457A, and JM0372.

4. Results

4.1. Petrography and Mineralogy of the Kindi Igneous Rocks

The Kindi anomaly lies over two granitic bodies surrounded by granodiorite (**Figure 1(c)**). These granitic bodies are composed of two petrographic facies: a porphyroid biotite granite that locally transitions into a leucogranite, and a medium-grained biotite granite. The contact of these formations, located to the north of the anomaly in the Siglé area, exposes an association of a granitic augen orthogneiss and a fine-grained biotite granite. The entire area is intruded by a complex network of dykes and veins, including microdiorite, microgranite, pegmatite/aplite, and quartz veins. Only medium-grained biotite granite and, to a lesser extent, porphyroid biotite granite, granodiorite, granitic augen orthogneiss, leucogranite, aplitic granite, and pegmatite were sampled to perform whole-rock geochemical analysis.

4.1.1. Granodiorite

Granodiorite is less common in the study area and spatially occurs as slabs. It is a heterogeneous rock, enclosing biotite-rich schlieren and/or dark fusiform enclaves of xenoliths, the largest of which are 4 to 5 m long and 40 cm wide. It is crosscut by aplite veins (less than 1 m in thickness) of granitic composition and quartz veinlets (less than 5 cm in thickness). Granodiorite consists mainly of plagioclase (30%), quartz (20%), K-feldspar (15%), green-brown biotite (20%) and hornblende-type amphibole (10%). It also contains sphene, epidote, iron and/or

titanium oxides, zircon and apatite. It has a medium-grained to porphyritic hypidiomorphic texture. The medium-grained grey facies is cataclastic to more-or-less microbrecciated. It displays a dense network of intra- to intercrystalline microfractures, largely obliterating the primary texture. The porphyritic facies shows incipient foliation planes underlined by the alignment of small ferromagnesian minerals (biotite-epidote in particular) and protoclastic-type deformation planes. The more-or-less cataclastic minerals are locally truncated feldspar phenocrysts and recrystallized quartz.

4.1.2. Medium-Grained Biotite Granite

It outcrops over more than 1 km^2 in the form of rock-block domes of varying sizes, locally evolving into tors (**Figure 2(a)**). It is composed of a main grey facies to a locally ocher facies granite that is typically characterized by a secondary hematitization related to fracturing of the joint network (**Figure 2(b)**) and is often injected with pegmatite and quartz veins. This granite is rich in ferromagnesian minerals compared to porphyroid biotite granite and exhibits a hetero-granular texture with K-feldspar phenocrysts (orthose) (0.5% - 1.4% An, 2.6% - 3.9% Ab, 96.1% - 97.3% Or), in particular oligoclase (16.3% - 17.8% An, 81.2% - 83.4% Ab, 0.2% - 1.0% Or) (**Table 1**, **Figure 2(c)** & **Figure 3(a)**) and ferric biotite (22.3% - 22.7% FeOt,

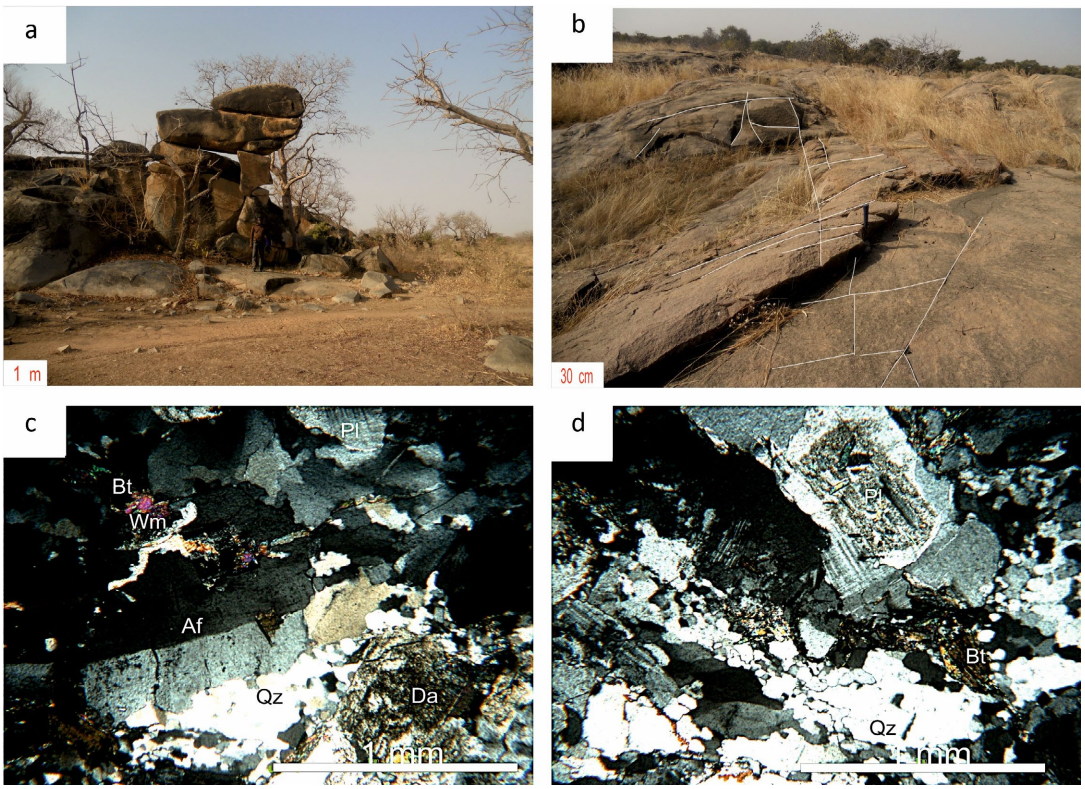

Figure 2. Photographs of medium-grained biotite granite showing macroscopic and microscopic characteristics. (a) Granitic tors; (b) Fractured joint network hosted in red ochre, medium-grained biotite granite facies; (c) Photomicrograph displays mineralogical components of the medium-grained biotite granite; (d) Cataclastic facies of the medium-grained biotite granite. Bt: Biotite, Da: Damourite, Pl: Plagioclase, Wm: Muscovite, Qz: Quartz.

Table 1. Chemical composition in major elements (wt%) and atoms per formula unit (apfu) composition of feldspars from porphyroid biotite granite and medium-grained biotite granite.

Rocks	Porphyroid biotite granite										Medium-grained biotite granite									
Samples	PI04-A	PI04-A	PI04-A	PI 05-C	PI 05-C	PI04-A	PI04-A	PI04-A	PI 05-C	PI 05-C	PI 05-C	PI 08-B	PI 08-B	PI 08-B	PI 08-B	PI 08-B	PI 08-B	PI 08-B	PI 08-B	PI 08-B
Minerals	K-feldspars						Plagioclase					K-feldspars				Plagioclase				
Mark	1	2	3	4	5	1	2	3	4	5	6	1	2	1	2	2	3.	4		
SiO_2	64.259	64.384	64.688	63.705	64.898	65.532	65.206	64.107	64.446	64.6502	64.279	64.389	64.169	64.376	64.921	64.937	100.259			
MgO	0.0088	0.0024	-	0.0088	0.0056	-	0.0017	0.0186	-	-	0.0093	0.0064	0.0104	-	-	-	-			
FeOt	0.0543	0.0474	0.014	-	0.0227	0.0775	-	-	0.0492	0.0053	0.1899	0.2011	0.007	0.0703	0.0706	-	0.0018			
Na_2O	0.492	0.2714	0.618	0.4678	0.4503	10.419	10.076	9.5523	9.5321	9.4666	9.3812	0.3089	0.4575	9.7677	9.4953	9.6361	-			
Al_2O_3	18.423	18.148	18.499	17.97	17.814	21.339	22.178	22.452	22.164	21.5924	21.892	18.321	18.273	22.506	22.21	22.296	0.0039			
K_2O	16.499	16.54	16.124	16.183	16.679	0.0876	0.2278	0.1105	0.0856	0.145	0.1558	16.292	16.35	0.1074	0.1689	0.0407	0.0128			
CaO	0.0048	0.0323	-	-	-	2.4018	2.2754	3.692	3.5485	3.437	3.5869	0.0113	0.0016	3.5458	3.5445	3.2114	-			
MnO	0.0008	0.0181	-	0.0192	0.0027	0.011	-	0.0079	-	-	0.022	-	-	-	0.0095	-	0.0497			
TiO_2	0.0262	0.0936	0.0637	-	0.0056	0.0074	-	-	-	-	-	0.0149	-	0.0186	-	0.0149	0.0131			
Cr_2O_3	-	0.0344	-	-	0.0074	0.0221	0.0245	0.0049	0.027	0.0368	0.0442	0.0123	-	0.0319	-	0.0148	-			
Total	99.767	99.572	100.01	98.354	99.885	99.898	99.989	99.946	99.852	99.3333	99.561	99.557	99.269	100.42	100.42	100.15	100.341			
Si	11.942	11.983	11.961	11.993	12.045	11.546	11.465	11.319	11.378	11.463	11.393	11.973	11.971	11.319	11.397	11.409	15.994			
Mg	0.002	0.001	-	0.002	0.002	-	-	0.005	-	-	0.002	0.002	0.003	-	-	-	-			
Fe	0.008	0.007	0.002	-	0.004	0.011	-	-	0.007	0.001	0.028	0.031	0.001	0.010	0.010	-	-			
Na	0.177	0.098	0.222	0.171	0.162	3.559	3.435	3.270	3.263	3.254	3.224	0.111	0.165	3.330	3.232	3.282	-			
Al	4.035	3.981	4.031	3.987	3.897	4.431	4.596	4.672	4.612	4.512	4.573	4.015	4.017	4.664	4.595	4.617	0.001			
K	3.912	3.927	3.803	3.887	3.949	0.020	0.051	0.025	0.019	0.033	0.035	3.865	3.891	0.024	0.038	0.009	0.003			
Ca	0.001	0.006	-	-	-	0.453	0.429	0.698	0.671	0.653	0.681	0.002	-	0.668	0.667	0.605	-			
Mn	-	0.003	-	0.003	-	0.002	-	0.001	-	-	0.003	-	-	-	0.001	-	0.007			
Ti	0.004	0.013	0.009	-	0.001	0.001	-	-	-	-	-	0.002	-	0.002	-	0.002	0.002			
Cr	-	0.005	-	-	0.001	0.003	0.003	0.001	0.004	0.005	0.006	0.002	-	0.004	-	0.002	-			
Total	20.081	20.024	20.027	20.042	20.061	20.026	19.979	19.992	19.955	19.922	19.947	20.004	20.049	20.022	19.940	19.926	16.006			
An	-	0.2	-	-	-	11.8	11.5	18.4	17.8	17.4	18.1	0.1	-	17.4	17.8	16.3	-			
Ab	4.1	2.3	5.2	4.0	3.7	87.6	87.1	81.0	81.7	81.7	80.9	2.6	3.9	81.9	81.2	83.4	-			
Or	95.9	97.5	94.8	96.0	96.3	0.5	1.4	0.7	0.5	0.9	0.9	97.3	96.1	0.6	1.0	0.2	100.0			

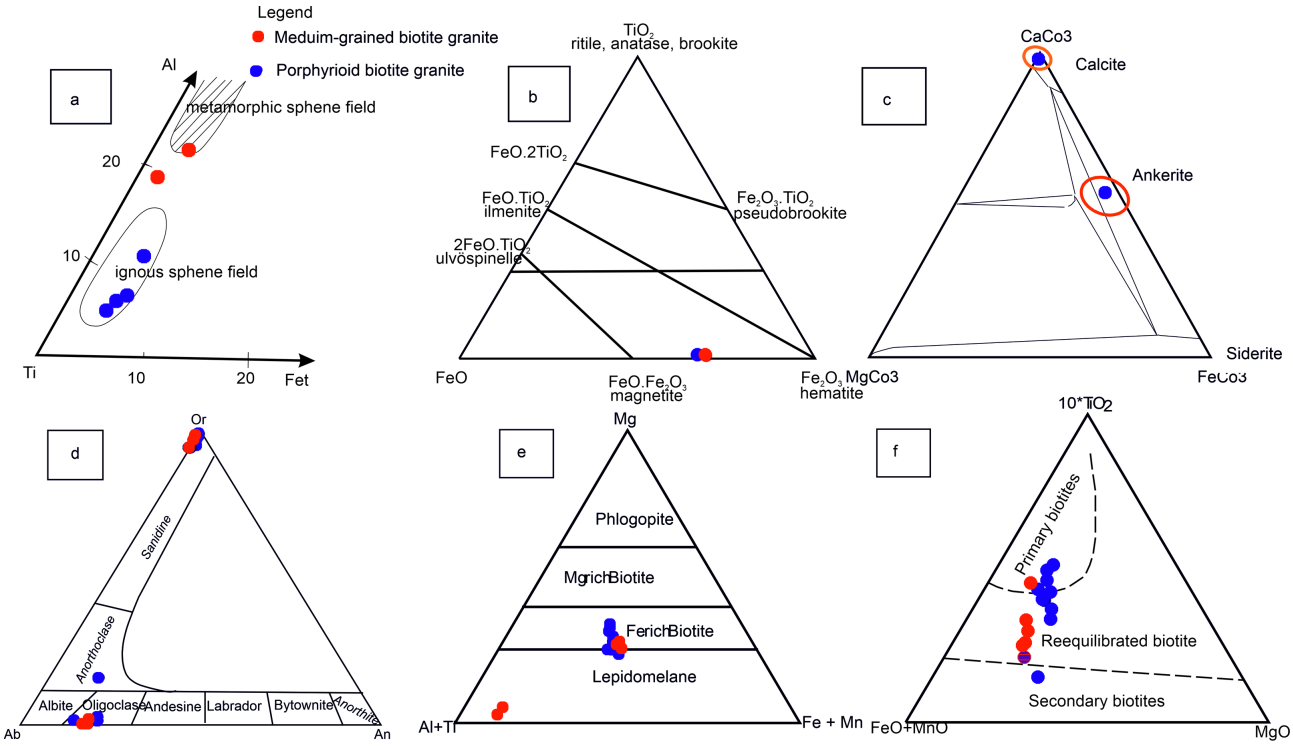

Figure 3. Geochemical composition of minerals from porphyroid biotite granite and medium-grained biotite granite, in ternary diagrams. (a) Feldspar compositions plotted on the Ab-Or-An diagram, Or: orthose, Ab: albite, An: anorthite; (b) Composition of biotites in the Mg-Al + Ti-Fe + Mn diagram [22]; (c) Composition of titanite in the Al-Ti-Fe(t) diagram [23]; (d) Composition of biotites in the 10*TiO_2-FeO+MnO-MgO diagram [24]; (e) Composition of oxides in the TiO_2-Fe_2O_3-FeO diagram [25] and (f) Composition of carbonates in the $CaCO_3$-$FeCO_3$ and $MgCO_3$ diagram [26].

8.4717% - 9.0867% MgO, 15.11 - 15.77 Al_2O_3) altered into alumino-titanium muscovite (5.42 - 5.49 FeOt, 1.59% - 1.86% MgO, 28.45 - 29.04 Al_2O_3) (**Table 2**, **Figure 3(b)**). It contains an accessory mineral assemblage of coarse sphene, epidote, zoned allanite surrounded by epidote, and opaque minerals in interstices or included in sphene crystals. Apart from its content in dark minerals higher than in the porphyroid biotite granite, it is also characterized by a cataclastic texture (**Figure 2(d)**), the presence of metamorphic sphene (**Figure 3(c)**) and re-equilibrated biotite by late hydrothermal fluids (**Figure 3(d)**). Locally, this biotite granite is foliated with a mylonitic texture.

4.1.3. Porphyroid Biotite Granite

It forms two NE-SW oriented and distinct massifs (**Figure 1(c)**) that outcrop as slabs (**Figure 4(a)**) or windows (50 m). This granite is of light gray color, with low ferromagnesian mineral content (less than 15 %), and rare mafic and surmicaceous enclaves that are ovoid or circumscribed in shape. It has a coarse-grained porphyroid texture (**Figure 4(b)**, **Figure 4(c)**), locally protomylonitized by late brittle deformation. It is composed of quartz, K-feldspar megacrysts (4 - 6 cm), zoned plagioclase (**Figure 4(d)**), biotite, and accessory igneous sphene (**Figure 3(c)**), epidote, allanite, opaque minerals such as hematite (63.10% - 66.39% Fe_2O_3) (**Table 3**, **Figure 3(e)**), zircon, and apatite. Chlorite, damourite, calcite

Table 2. Chemical composition of major elements (wt%) and atom per formula unit (apfu) composition of biotite and muscovite from porphyroid biotite granite and medium-grained biotite granite.

Rocks	Porphyroid biotite granite									Medium-grained biotite granite								
Samples	PI04-A	PI04-A	PI04-A	PI04-A	PI04-A	PI 05-C	PI 05-C	PI 05-C	PI 15	PI 15	PI 08-B	PI 08-B	PI 08-B	PI 08-B	PI 08-B	PI 08-B	PI 08-B	PI 08-B
Minerals	Biotite											Biotite					Muscovite	
Mark	1	2	3	4	5	6	7	8	9	10	1	2	3	4	5	6		
SiO_2	36.542	36.354	36.9	36.496	36.903	37.183	37.336	37.457	37.44	36.681	36.898	36.997	36.819	36.47	46.53	46.718		
MgO	9.548	8.2823	9.352	8.9678	8.8355	10.353	10.502	10.912	9.774	10.446	9.0867	8.4717	8.7013	8.7615	1.8672	1.5925		
FeO_t	20.486	22.064	21.28	20.145	21.091	18.94	18.707	19.175	20.28	20.058	22.347	22.87	22.639	22.767	5.4227	5.4909		
Na_2O	0.0049	0.0331	0.038	0.0244	0.0525	0.0096	0.0112	0.0288	0.064	0.0661	0.0443	0.0165	0.0182	0.0281	0.1866	0.1838		
Al_2O_3	15.479	15.378	15.15	16.076	14.783	16.264	15.325	14.799	14.16	14.498	15.776	15.525	15.307	15.111	28.451	29.045		
K_2O	10.175	9.6819	9.578	9.9541	9.9501	10.066	9.7701	9.8585	10.03	9.999	9.8571	9.8828	9.8629	9.7682	11.103	11.232		
CaO	0.0352	-	0.052	0.0153	0.0092	-	-	0.0384	0.009	-	-	0.0184	-	0.0613	0.0142	-		
MnO	0.3448	0.4197	0.332	0.4813	0.5194	0.4909	0.3927	0.4124	0.671	0.686	0.3072	0.2368	0.2166	0.2799	0.0128	-		
TiO_2	2.0923	2.4327	2.167	2.6376	3.0661	0.5859	1.8038	1.6313	3.329	2.3799	0.941	1.1283	1.4145	1.1924	0.3841	0.6056		
Cr_2O_3	0.0433	-	-	-	-	-	-	0.0137	0.021	-	-	0.0363	0.0159	0.0045	0.0144	0.0192		
Total	94.75	94.646	94.84	94.797	95.209	93.892	93.849	94.326	95.78	94.814	95.257	95.183	94.994	94.444	93.987	94.888		
Si	5.668	5.676	5.715	5.639	5.709	5.756	5.770	5.780	5.740	5.685	5.720	5.753	5.735	5.726	6.456	6.423		
Mg	2.208	1.928	2.159	2.066	2.038	2.389	2.420	2.510	2.234	2.413	2.100	1.964	2.020	2.051	0.386	0.326		
Fe	2.657	2.881	2.756	2.603	2.729	2.452	2.418	2.475	2.599	2.600	2.897	2.974	2.949	2.990	0.629	0.631		
Na	0.001	0.010	0.011	0.007	0.016	0.003	0.003	0.009	0.019	0.020	0.013	0.005	0.005	0.009	0.050	0.049		
Al	2.830	2.830	2.765	2.927	2.695	2.967	2.791	2.692	2.558	2.648	2.882	2.845	2.810	2.796	4.652	4.706		
K	2.013	1.928	1.892	1.962	1.964	1.988	1.926	1.941	1.962	1.977	1.949	1.961	1.960	1.957	1.965	1.970		
Ca	0.006	-	0.009	0.003	0.002	-	-	0.006	0.002	-	-	0.003	-	0.010	0.002	-		
Mn	0.045	0.055	0.044	0.063	0.068	0.064	0.051	0.054	0.087	0.090	0.040	0.031	0.029	0.037	0.002	-		
Ti	0.244	0.286	0.252	0.307	0.357	0.068	0.210	0.189	0.384	0.278	0.110	0.132	0.166	0.141	0.040	0.063		
Cr	0.005	-	-	-	-	-	-	0.002	0.002	-	-	0.004	0.002	0.001	0.002	0.002		

Continued

Si + Al	8.000	8.000	8.000	8.000	8.000	8.000	8.000	8.000	8.000	8.000	8.000	8.000	8.000	8.000	8.000	8.000
Al	0.50	0.51	0.48	0.57	0.40	0.72	0.56	0.47	0.30	0.33	0.60	0.60	0.55	0.52	3.11	3.13
Mg	2.2	1.9	2.2	2.1	2.0	2.4	2.4	2.5	2.2	2.4	2.1	2.0	2.0	2.1	0.4	0.3
Fe	2.7	2.9	2.8	2.6	2.7	2.5	2.4	2.5	2.6	2.6	2.9	3.0	2.9	3.0	0.6	0.6
Mn	0.0	0.1	0.0	0.1	0.1	0.1	0.1	0.1	0.1	0.1	0.0	0.0	0.0	0.0	0.0	-
Ti	0.244	0.286	0.252	0.307	0.357	0.068	0.210	0.189	0.384	0.278	0.110	0.132	0.166	0.141	0.040	0.063
Cr	0.005	-	-	-	-	-	-	0.002	0.002	-	-	0.004	0.002	0.001	0.002	0.002
Ca	0.006	-	0.009	0.003	0.002	-	-	0.006	0.002	-	-	0.003	-	0.010	0.002	-
Na	0.001	0.010	0.011	0.007	0.016	0.003	0.003	0.009	0.019	0.020	0.013	0.005	0.005	0.009	0.050	0.049
K	2.013	1.928	1.892	1.962	1.964	1.988	1.926	1.941	1.962	1.977	1.949	1.961	1.960	1.957	1.965	1.970
Al + Mg + Fe_ Mn + Ti + Cr	5.66	5.66	5.69	5.61	5.60	5.70	5.66	5.70	5.60	5.71	5.75	5.70	5.71	5.74	4.17	4.15
Ca + Na + K	2.020	1.938	1.912	1.972	1.982	1.991	1.929	1.956	1.983	1.997	1.962	1.969	1.965	1.976	2.017	2.019

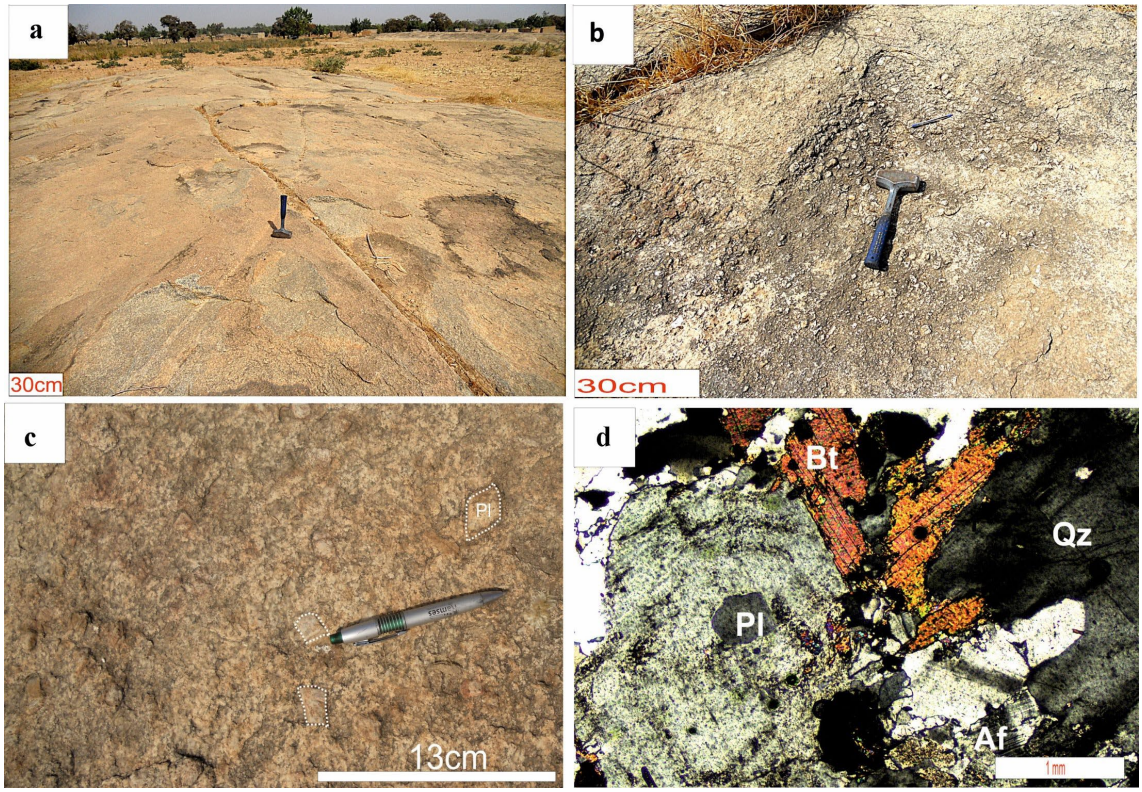

Figure 4. Photographs of porphyroid biotite granite. (a) Slab outcrop; (b) Pegmatitic facies associated with porphyroid granite; (c) Protomylonitic facies of the porphyroid biotite granite; (d) Zoned plagioclase associated with biotite and quartz. Abbreviations: Af: alkali feldspar; Bt: biotite; Pl: plagioclase; Qz: quartz.

(55.81% CaO, 0.03% FeOt), and ankerite (12.687% CaO, 12.79% FeOt) (**Table 3**, **Figure 3(f)**) also occur as hydrothermal secondary alteration minerals. The phenocrysts are represented by K-feldspars as microcline, orthose, and anorthose types (**Figure 3(a)**). Plagioclase occurs in a heterogranular texture with variable sizes from 0.2 to 3 mm, sometimes cracked and damouritized, with minor quartz inclusions. Plagioclase is also found as inclusions in K-feldspar, developing a myrmekitic texture at its interface. It has an oligoclase composition (18.4% - 11.5% An, 87.1% - 81.7% Ab, 1.4% - 0.5% Or) (**Table 1**) and rarely anorthoclase. Biotite is ferroan (**Figure 3(b)**), varies between 10% and 15%, and contains inclusions of zircon, sphene, apatite, opaque minerals, and zoned allanite. Mainly primary or scarcely re-equilibrated by late hydrothermal fluids (**Figure 3(d)**), biotite is often altered into chlorite and illite/muscovite. Potential uraniferous accessory minerals may include allanite, sphene, zircon, and apatite [27].

4.1.4. Augen Granitic Orthogneiss

It has a fine-grained gneissic texture with frequent feldspar lenses. The texture is grano-lepidoblastic, with fine grains (0.5 mm) of K-feldspar (orthoclase, microcline), plagioclase, and quartz layers, alternating with dark, fine-grained beds dominated by greenish and brownish-green biotite/chlorite. Major accessory minerals include sphene and epidote.

Table 3. Chemical composition in major elements (wt%) and atoms per formula unit (apfu) composition of sphene, opaque, and carbonate from porphyroid biotite granite and medium-grained biotite granite.

Rocks	Porphyroid biotite granite							Medium-grained biotite granite						
Samples	PI04-A	PI 05-C	PI 05-C	PI 15	PI04-A	PI04-A	PI04-A	PI04-A	PI 05-C	PI 08-B	PI 08-B	PI 08-B	PI 08-B	PI 08-B
Minerals	Sphene				Opaque		Carbonate			Sphene		Opaque		
Mark	1	2	3	4	1	2	1	2	1	2	1	2	1	2
SiO_2	30.3385	29.869	30.0529	30.13	0.2575	0.0546	30.42	0.0836	30.6322	30.4957	-	-	-	-
MgO	0.0303	0.0507	0.0391	-	0.0277	0.0224	0.686	0.0056	0.03	0.076	-	-	-	-
FeOt	1.7229	1.9587	1.7943	1.538	86.0265	89.6883	12.795	0.0274	1.6386	1.8906	91.8583	92.6805		
Na_2O	0.0299	0.1217	0.0943	0.012	-	0.0623	0.1271	0.0967	0.0327	0.0182	0.0207	-		
Al_2O_3	2.9818	1.8119	1.5355	1.338	0.0708	-	11.198	0.0504	5.8401	4.8753	0.025	0.0102		
K_2O	0.0082	0.0867	0.0358	-	-	-	0.0496	0.0245	0.0083	0.0028	0.0026	0.0264		
CaO	27.747	20.259	26.9831	27.07	0.0224	0.0276	12.687	55.81	28.4406	28.231	0.0275	0.0157		
MnO	0.1648	0.1809	0.0918	0.089	0.0444	0.07	0.3568	0.0993	0.1269	0.0972	0.0264	0.0348		
TiO_2	34.9837	36.051	35.6109	36.53	0.165	0.0523	0.8892	-	29.8905	31.8197	0.0566	0.0189		
Cr_2O_3	0.0131	0.0024	0.0171	0.051	0.0501	0.0133	-	0.0221	-	0.0243	0.207	0.2369		
Total	98.0456	90.391	96.2548	96.76	86.6645	89.9908	69.2088	56.219	96.6399	97.5306	92.2243	93.0233		
Si	4.045	4.239	4.086	4.071	0.011	0.002	0.565	0.003	4.123	4.078	-	-		
Mg	0.006	0.011	0.008	-	0.002	0.001	0.019	-	0.006	**0.015**	-	-		
Fe	0.192	0.232	0.204	0.174	(2.975)	(2.989)	0.199	0.001	0.184	0.211	-2.988	(2.989)		
Na	0.008	0.033	0.025	0.003	-	0.005	0.005	0.006	0.009	0.005	0.002	-		
Al	0.469	0.303	0.246	0.213	0.003	-	0.245	0.002	0.926	0.768	0.001	-		
K	0.001	0.016	0.006	-	-	-	0.001	0.001	0.001	-	-	0.001		
Ca	3.964	3.080	3.931	3.918	0.001	0.001	0.252	1.983	4.101	4.045	0.001	0.001		
Mn	0.019	0.022	0.011	0.010	0.002	0.002	0.006	0.003	0.014	0.011	0.001	0.001		
Ti	3.509	3.849	3.643	3.713	0.005	0.002	0.012	-	3.027	3.201	0.002	0.001		
Cr	0.001	-	0.002	0.005	0.002	-	-	0.001	-	0.003	0.006	0.007		

Continued

Cations			1.303	2.000		
Total	3.000	3.003			3.001	3.001
Fe_2O_3	63.10	66.39			67.95	68.60
FeO	29.25	29.95			30.72	30.95
Tot. rec	92.99	96.64			99.04	99.89
Fe^{3+}	1.963	1.991			1.989	1.991
Fe^{2+}	1.011	0.998			0.999	0.998
[Mg]	0.10	-			-	-
a	0.001	-			0.003	0.004
b	0.002	-			0.001	-
g	0.997	1.000			0.996	0.996
XFe/XMg	592.39	750.08			∞	∞
$Ti/Ti^{+}Al^{+}Cr$	0.502	0.789			0.181	0.067
$Fe^{2}/Fe^{2+}Mg$	99.8	99.9			100	100
Cr/Cr+Al	0.322	1.000			0.847	0.940
$Fe^{3}/Fe^{3+}Al^{+}Cr$	0.997	1.000			0.996	0.996

4.1.5. Leucogranite

The leucogranite occurs as elongated bands, more or less individualized, and associated with the porphyroid biotite granite. It exhibits two sub-facies: (i) a medium-grained and heterogranular biotite-dominated with minor muscovite leucogranite that accessorily contains allanite and opaque minerals, and (ii) a fine-grained two-mica (biotite and muscovite) leucogranite.

4.1.6. Fine-Grained Biotite Granite

The fine-grained biotite occurs as elongated bands of metric extension, oriented N60. It is intruded by parallel pegmatite veins of 10 cm to 1 m in thickness. It is a leucocratic granite with an isogranular texture and a discretely oriented structure.

4.1.7. Dyke and Vein Systems

The dyke and vein system intersecting the country rocks is composed of microdiorite and microgranite, granitic aplites, pegmatites, and quartz veinlets of centimetric to decimetric thickness (**Figure 5(a)**).

The microdiorite is associated with the microgranite; they form a dyke system preferentially localized at the contact between the porphyroid biotite granite and the fine-grained granite. Both are less common and richer in ferromagnesian minerals than the latter, and are recognized by their microgranular and porphyritic textures.

The aplitic granite is frequently associated with pegmatite veins in the biotite porphyroid granite (**Figure 5(b)**). It has a microgranular and sub-isogranular texture and is composed of abundant quartz, plagioclase, K-feldspar, and accessory biotite, epidote, sphene, allanite, zircon, chlorite, muscovite, and secondary opaque minerals. The rock is weakly affected by plastic to cataclastic deformation, which is accompanied by hydrothermal alteration.

The pegmatite crosscuts all the granitic units as veins with thicknesses of metric order. This rock is leucocratic with a very coarse-grained texture consisting of subautomorphic to automorphic megacrysts of centimeter-sized feldspar (FK > PL). The phases observed macroscopically are mainly potassium feldspars in

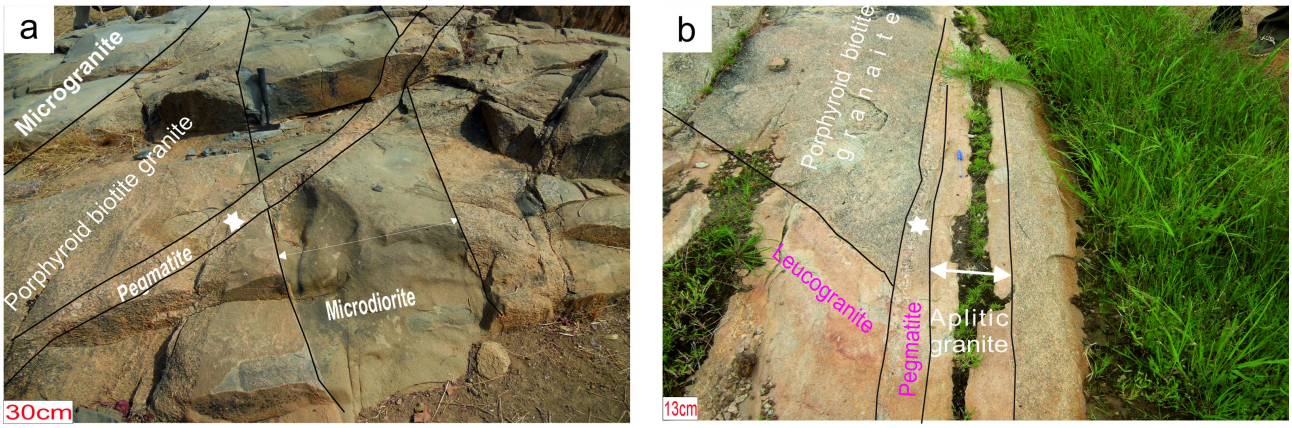

Figure 5. Photographs of the vein system. (a) Porphyroid biotite granite crosscut by microdiorite, microgranite, and pegmatite veins; (b) Porphyroid biotite granite associated with a leucogranite, both crosscut by aplite and pegmatite dykes.

coarse crystals (0.8 to 1.4 cm × 1.4 to 1.9 cm) of a pinkish color, plagioclases, abundant quartz, and, rarely, lamellae of more or less altered biotite. Under the microscope, it contains cataclased or plastically deformed minerals, specifically plagioclase, which frequently exhibits twisted twinning.

Quartz veinlets are rare and generally associated with medium-grained biotite granite.

4.2. Accessory Minerals

In the Kindi granitoids, accessory minerals vary in nature, form, and quantity (Table 4) and mainly include sphene, zircon, allanite, epidote, apatite, magnetite, and/or hematite, among which allanite, sphene, and zircon may host a significant amount of uranium that could be liberated into the rock through the metamictization process (*i.e.*, destruction of the mineral's structure due to radiation effects) and remobilized during post-crystallization hydrothermal alteration.

Table 4. Relative abundance of uranium-rich accessory minerals in the Kindi anomaly.

Mineral/Rock	Granodiorite	Medium-grained biotite granite	Porphyroid biotite granite	Orthogneiss	Leucogranite	Aplitic granite	Pegmatite
Opaques	X	X	XX	X	XX	XX	X
Sphene	X	XX	X	XX	XX	X	
Allanite	X	X	X	X	XX	XX	
Zircon	XX	XX	XX	X	X	X	X
Uranitite	?	?	?		?	?	?
Rutile	X	X	X				
apatite	X	X	XX			X	
Epidote	XX	X	XX	XX			

Heterometric rhombic sphene (Figure 6(a)) is found as an inclusion in the biotite, or in interstitial form, sometimes filled with small inclusions of zircon or opaque minerals, sometimes haloed, and very often with a metamict texture (Figure 6(b)); it is also one of the destabilisation products of the biotite. It is more common in medium-grained granite, leucogranite, and aplitic granite (Table 4).

Fine to coarse zircon is present in all facies in varying quantities. It is sometimes zoned or often found as inclusions in biotite and felsic minerals, regularly accompanied by an alteration halo.

Allanite occurs as fine or coarse crystals in automorphic form (Figure 6(c)). It occurs in inclusions, sometimes zoned, with a discrete alteration halo (Figure 6(c)), or in a metamict texture characterized by a mineral destruction halo (Figure 6(d)). It is less frequent than the previous zircon and sphene. At the contact with the plagioclase, an epidote halo develops.

The automorphic epidote (Figure 6(c)) is probably deuteric and contains inclusions of zircon or felsic minerals.

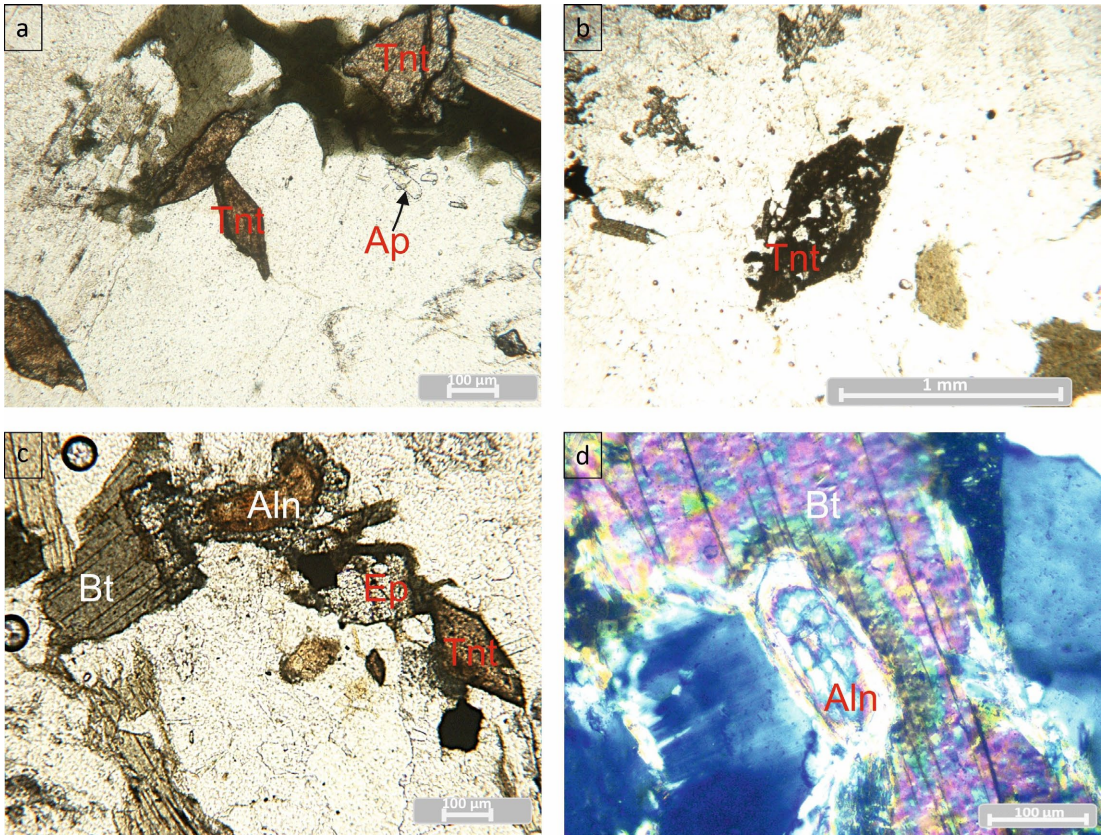

Figure 6. Microphotographs of accessory phases in granites from the Kindi region under natural and polarised light. (a) Rhombic sphenes, sometimes included in the biotite of porphyroid biotite granite; (b) Metamict sphene in medium-grained biotite granite; (c) Zoned allanite included in the biotite of porphyroid biotite granite; (d) Metamict allanite included in the biotite of porphyroid biotite granite. Aln: allanite, Bt: biotite, Ep: epidote, Hem: hematite, Tnt: sphene.

Opaque crystals represented by magnetite and hematite are sometimes subautomorphic, isolated, in clusters, or as inclusions in felsic minerals, or in the form of interstitial xenomorphs or honeycomb crystals trapping carbonates. These opaques also result from the alteration of biotite, sometimes associated with muscovite. Some crystals exhibit halos of epidote, carbonate, or symplectic quartz in contact with biotite or plagioclase.

4.3. Secondary Minerals

The secondary mineral assemblage (Table 5) is composed of a first generation of secondary alteration phases developed in situ from the major silicates of the granitoids, and a second alteration phase, which is controlled by the circulation of hydrothermal fluids along the fracturing system of the rocks, is superimposed on the first.

Plagioclase was replaced by sericite ± clay or muscovite and epidote ± carbonate, or symplectite epidote and quartz. Orthoclase often alters into muscovite and secondary quartz, while biotite changes to chlorite or muscovite. Sericite alteration locally affects the plagioclase, as does clay or carbonate alteration.

Table 5. Index of hydrothermal alteration phases in the granites of the Kindi anomaly.

Mineral/Rock	Granodiorite	Medium-grained biotite granite	Porphyroid biotite granite	Orthogneiss	Leucogranite	Aplitic granite	Pegmatite
Muscoviste		X	X	X	X	X	X
Sericite	X	X	X	X		X	X
Clay	X		X	X		X	
Chlorite	X	X	X	X		X	
Biotite			X	X		X	
Epidote	X	X	X	X	X	X	
Carbonates	X		X	X	X	X	
Secondary quartz		X					X
Oxides	X	X	X	X			

The medium-grained granite is frequently fractured, with infilling of secondary quartz and muscovite displaying greisenization [28]. The cracks of the potassic feldspars, which seem like adularia, are filled by crystallization of secondary brown biotite, sometimes replacing the chloritized biotite (**Figure 7(a)**), revealing potassic alteration [29]. This alteration sometimes involves the digestion of certain portions of the large patches of these feldspars and biotite (**Figure 7(b)**).

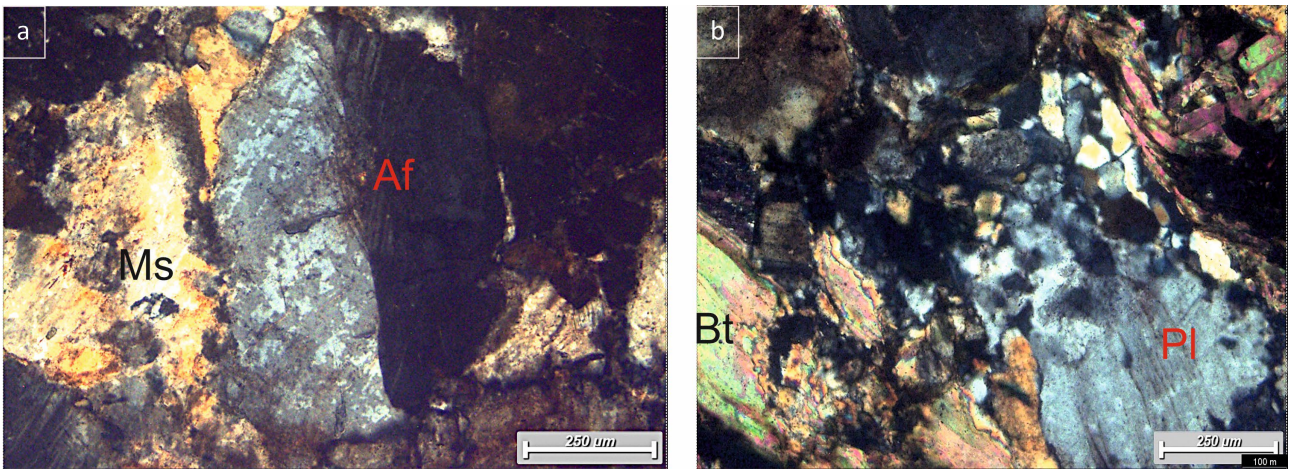

Figure 7. Microphotographs of hydrothermal alteration phases from biotite medium-grained granite: (a) microperthitic orthoclase; (b) feldspar and biotite digestion. Bt: Biotite; Af: Orthoclase; Chl: Chlorite; Pl: Plagioclase; Qz: Quartz.

Cracks and brecciated zones in porphyroid biotite granite are filled with phyllites dominated by muscovite and chlorite, associated with epidote and carbonates (**Figure 8(a)**), recorded as propylitic alteration [29]. This alteration is pointed out by the changes of biotite in this rock to chlorite, epidote, carbonate, and Fe-oxides (**Figure 8(b)**) in the porphyroid biotite granite and granodiorite/trondhjemite facies.

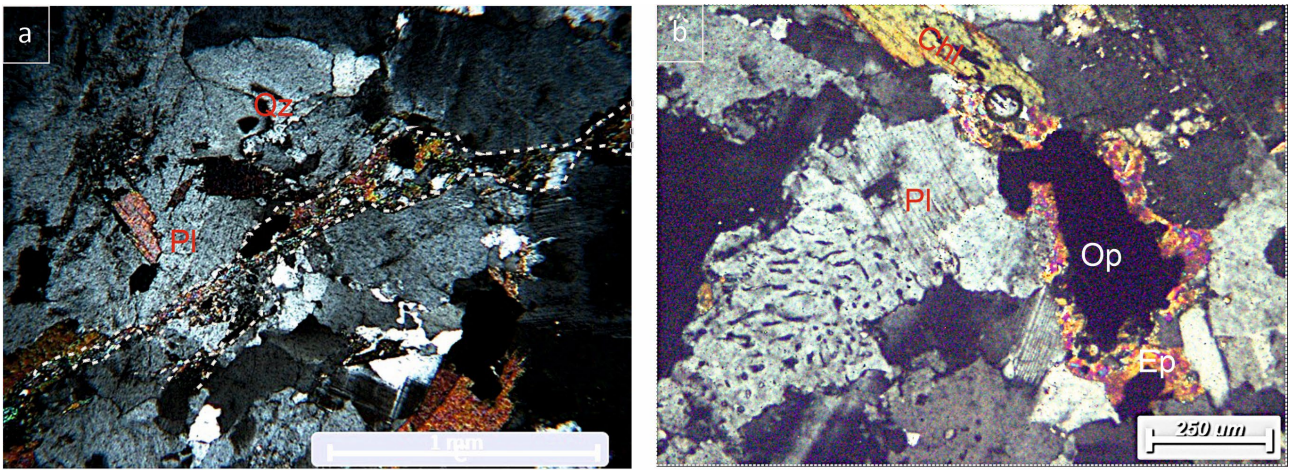

Figure 8. Microphotographs of secondary phases resulting from hydrothermal alteration of porphyroid biotite granite: (a) a microcrack filled with phyllites and carbonates, and (b) destabilisation of biotite into chlorite-epidote-opaque and plagioclase into myrmekites. Cb: carbonate; Bt: biotite; Myk: myrmekite; Chl: chlorite; Op: opaque; Pl: plagioclase; Qz: quartz.

4.4. Whole-Rock Geochemistry

Classification and Geochemical Characteristics of the Kindi Igneous Rocks

Geochemical data on major, trace, and rare-earth elements of granitoids from the Kindi radiometric anomaly are reported in Table 6 and Table 7.

Table 6. Major elements of granitoids in the Kindi area.

Lithology	Granodiorite		Medium-grained biotite granite		Porphyroid biotite granite					Orthogneiss granite	Leuco-granite	Aplitic granite	Pegmatite
Sample	PC0334	JM0372	PC0335A	PC0343	PI05C	PI15	PI04B	PC0457A	PI04A	PI07B	PC0335B	PI05A	PI07C
Majors elements (%)													
SiO_2	65.03	68.94	69.39	69.27	72.15	71.97	73.81	72.91	74.39	72.60	73.70	75.66	70.32
TiO_2	0.72	0.31	0.48	0.68	0.26	0.25	0.21	0.22	0.18	0.18	0.13	0.07	0.01
Al_2O_3	15.67	15.27	14.47	14.41	14.20	14.26	13.75	14.12	14.34	14.66	14.16	13.65	15.94
Fe_2O_3	4.18	2.90	2.90	2.81	1.96	1.98	1.65	1.35	1.44	1.39	1.05	0.85	0.45
MnO	0.09	0.06	0.04	0.04	0.04	0.03	0.03	0.02	0.02	0.03	0.02	0.05	<0.01
MgO	2.19	1.52	1.11	0.80	0.62	0.67	0.39	0.41	0.33	0.38	0.16	0.08	0.05
CaO	3.87	3.04	2.23	2.06	1.76	1.83	1.40	1.27	1.40	1.41	1.26	0.92	0.19
Na_2O	5.10	4.41	4.05	3.59	3.96	3.96	3.84	3.56	3.52	4.64	4.31	4.33	2.78
K_2O	2.04	2.63	4.14	4.99	4.15	4.06	4.25	5.21	5.21	3.80	4.16	4.42	9.79
P_2O_5	0.21	0.09	0.17	0.15	0.10	0.06	0.07	0.07	0.07	0.06	0.02	0.02	0.01
LOI	0.60	0.40	0.60	0.80	0.50	0.70	0.40	0.30	0.80	0.40	0.50	0.00	0.30
$NaO + K_2O$	7.14	7.04	8.19	8.58	8.11	8.02	8.09	8.77	8.73	8.44	8.47	8.75	12.57
Norm CIPW (%)													
Q	17.46	24.79	24.23	24.28	28.83	28.65	31.83	29.14	30.69	27.66	29.84	31.53	16.24

Continued

C	0.00	0.00	0.00	0.00	0.23	0.17	0.46	0.48	0.53	0.49	0.32	0.12	0.45
Or	12.06	15.54	24.47	29.49	24.53	23.99	25.12	30.79	30.79	22.46	24.58	26.12	57.86
Ab	43.16	37.32	34.27	30.38	33.51	33.51	32.49	30.12	29.79	39.26	36.47	36.64	23.52
An	13.84	14.10	9.08	8.47	8.08	8.69	6.49	5.84	6.49	6.60	6.12	4.43	0.88
Di	1.43	0.00	0.00	0.00	0.00	0.00	0.00	0.00	0.00	0.00	0.00	0.00	0.00
Hy	4.79	3.79	2.77	1.99	1.54	1.67	0.97	1.02	0.82	0.95	0.40	0.20	0.13
Il	0.19	0.13	0.09	0.09	0.09	0.06	0.06	0.04	0.04	0.06	0.04	0.11	0.01
Hm	4.18	2.90	2.90	2.81	1.96	1.98	1.65	1.35	1.44	1.39	1.05	0.85	0.45
Tn	1.52	0.28	0.62	0.55	0.00	0.00	0.00	0.00	0.00	0.00	0.00	0.00	0.00
Ru	0.00	0.13	0.18	0.41	0.22	0.22	0.18	0.20	0.16	0.15	0.11	0.01	0.00
Ap	0.50	0.21	0.40	0.36	0.24	0.14	0.17	0.17	0.17	0.14	0.05	0.05	0.02
Sum	99.12	99.18	99.00	98.82	99.21	99.08	99.41	99.15	100.91	99.16	98.98	100.06	99.55

Table 7. Trace and rare earth element composition of granitoids from the Kindi area.

Petrography	Granodiorite		Medium-grained biotite granite		Porphyroid biotite granite					Orthogneiss granite	Leuco-granite	Aplitic granite	Pegmatite
Sample	PC0334	JM0372	PC0335A	PC0343	PI05C	PI15	PI04B	PC0457A	PI04A	PI07B	PC0335B	PI05A	PI07C
Traces elements (ppm)													
Cs	8.00	1.20	7.50	1.90	8.00	8.90	3.50	2.80	7.00	4.30	3.30	11.80	12.80
Rb	131.20	95.60	132.40	211.80	184.10	199.50	150.00	138.20	178.70	142.20	117.80	364.20	415.70
Ba	560.00	698.00	1522.00	1232.00	1012.00	922.00	608.00	1185.00	1216.00	992.00	705.00	118.00	846.00
Sr	573.50	738.30	865.80	246.40	429.90	423.50	270.00	408.50	411.40	852.40	402.60	55.00	287.20
Th	4.60	9.30	10.70	13.90	12.70	12.20	8.10	8.50	11.50	7.50	10.00	24.00	2.40
U	4.80	2.40	4.90	2.80	6.10	3.40	1.90	0.80	3.20	5.80	8.30	10.90	1.60
Th/U	0.95	3.87	2.18	4.96	2.08	3.58	4.26	10.62	3.83	1.29	1.20	2.20	1.50
Ta	0.40	0.40	0.60	0.70	1.50	1.10	1.00	0.30	1.00	1.10	0.80	1.50	0.60
Nb	5.30	5.50	6.80	9.10	9.20	7.20	6.10	3.10	5.10	5.80	5.90	9.60	2.40
Hf	2.80	4.00	4.00	10.60	3.70	3.40	3.60	4.00	4.10	3.10	4.10	6.80	0.30
Zr	106.10	136.60	145.70	416.90	121.60	119.90	125.20	127.70	136.50	102.00	130.80	112.40	5.00
Y					11.00	7.60	6.70		7.10	6.40		27.40	2.90
V	74.00	46.00	43.00	29.00	23.00	25.00	14.00	15.00	15.00	16.00	8.00	<8	<8.00
Sc	5.00	4.50	3.50	3.60	3.00	4.00	2.00	1.00	2.00	2.00	1.70	3.00	<1.00
Co	12.20	0.00	6.00	4.90	54.00	38.70	71.50	2.50	42.90	103.00	1.00	55.50	50.20
Cr	20.00		17.00	18.00				8.00			2.00		
Ni	23.60	19.50	11.90	6.80	4.50	4.10	2.70	2.70	2.10	3.50	0.80	1.00	1.50
Ag	32.00	16.00	29.00	32.00	<0.10	<0.10	<0.10	21.00	<0.10	<0.10	16.00	<0.10	<0.10

Continued

As	2.00	1.00	2.00	2.00	<0.50	<0.50	<0.50	1.00	<0.50	<0.50	1.00	<0.50	<0.50
B	1.00	0.00	1.00	2.00	0.00	0.00	0.00	0.00	0.00	0.00	0.00	0.00	0.00
Be	2.00	1.00	2.00	3.00	2.00	2.00	1.00	1.00	2.00	2.00	3.00	3.00	1.00
Bi	0.09	0.03	0.13	0.06	4.50	0.20	<0.10	0.00	<0.10	<0.10	0.10	0.20	0.40
Br	48.00		27.00	39.00				130.00			13.00		
Cd	0.15	0.02	0.10	0.15	<0.10	<0.10	<0.10	0.08	<0.10	<0.10	0.12	<0.10	<0.10
Cl	4.00	5.00	2.00	4.00	0.00	0.00	0.00	14.00	0.00	0.00	1.00	0.00	0.00
Cu	14.05	20.89	18.37	11.90	12.40	10.70	8.20	1.76	2.90	11.00	1.80	2.40	2.40
Ga	19.10	3.70	19.10	22.30	18.40	18.90	16.20	18.40	16.00	19.10	17.80	20.70	18.20
Ge	0.20	0.00	0.20	0.20	0.00	0.00	0.00	0.10	0.00	0.00	0.10	0.00	0.00
Hg	5.00	5.00	0.00	0.00	<0.01	<0.01	<0.01	5.00	<0.01	<0.01	0.00	<0.01	<0.01
Li	113.30	29.80	103.80	79.30				31.70			48.70		
Mo	0.32	0.71	0.47	0.54	0.60	0.60	0.40	0.29	0.40	0.40	0.17	0.30	0.50
Pb	13.86	23.91	29.58	24.92	6.80	6.70	4.90	18.54	8.50	4.20	37.57	7.40	9.70
Sb	0.00	0.04	0.02	0.00	<0.10	<0.10	<0.10	0.00	<0.10	<0.10	0.00	<0.10	<0.10
Se	0.10	0.00	0.00	0.00	<0.50	<0.50	<0.50	0.00	<0.50	<0.50	0.00	<0.50	<0.50
Sn	2.00	0.00	1.00	3.00	2.00	1.00	<1.00	0.00	<1.00	<1.00	0.00	2.00	<1.00
Tl	0.00	0.00	0.00	0.00	0.60	0.70	0.30	0.00	0.20	0.40	0.00	0.10	<0.10
Zn	66.80	34.50	58.70	75.80	49.00	47.00	39.00	38.20	30.00	41.00	26.90	31.00	4.00
Th/Ta	11.50	23.25	17.83	19.86	8.47	11.09	8.10	28.33	11.50	6.82	12.50	16.00	4.00
La/Nb	5.43	5.49	6.37	8.73	3.66	4.31	4.13	10.61	7.88	6.31	3.36	1.30	1.21
Rare earth elements (ppm)													
La	28.80	30.20	43.30	79.40	33.70	31.00	25.20	32.90	40.20	36.60	19.80	12.50	2.90
Ce	59.50	59.70	92.00	152.50	73.20	56.50	53.60	57.60	70.70	54.40	50.30	28.80	3.70
Pr	7.40	7.53	10.30	16.63	7.15	5.39	4.49	5.49	7.01	6.95	5.09	3.41	0.52
Nd	28.80	29.60	39.10	57.10	22.20	16.70	12.80	18.00	20.40	21.10	18.30	13.20	1.70
Sm	4.40	4.40	6.20	7.30	4.36	2.89	2.07	2.00	3.10	3.59	2.40	4.35	0.39
Eu	1.44	1.00	1.45	1.26	0.83	0.61	0.43	0.54	0.57	0.95	0.50	0.24	0.15
Gg	2.59	2.56	2.72	3.35	3.15	2.04	1.32	0.89	2.17	2.42	1.27	4.77	0.36
Tb	0.28	0.38	0.34	0.43	0.45	0.29	0.19	0.06	0.28	0.29	0.14	0.82	0.05
Dy	1.43	1.48	1.82	1.96	2.00	1.36	0.76	0.52	1.25	0.99	0.81	4.23	0.21
Ho	0.21	0.26	0.24	0.31	0.39	0.24	0.19	0.07	0.24	0.19	0.19	0.94	0.06
Er	0.61	0.71	0.67	0.76	1.12	0.75	0.43	0.22	0.77	0.53	0.56	2.67	0.19
Tm	0.08	0.10	0.07	0.09	0.15	0.11	0.08	0.00	0.10	0.07	0.09	0.38	0.04
Yb	0.60	0.70	0.63	0.64	1.05	0.81	0.47	0.20	0.76	0.39	0.72	2.58	0.18

Continued

Lu	0.07	0.08	0.08	0.09	0.15	0.1.0	0.07	0.04	0.09	0.07	0.12	0.36	0.03
Sum_REE	136.21	138.70	198.92	321.82	149.90	118.69	102.10	118.78	147.64	128.54	100.29	79.25	10.30
Eu/Eu*	1.30	0.91	1.08	0.78	0.68	0.77	0.79	1.24	0.67	0.98	0.87	0.16	1.22
LaN/SmN	4.10	4.30	4.38	6.81	4.84	6.72	7.63	10.31	8.12	6.39	5.17	1.80	4.66
LaN/YbN	32.67	29.36	46.77	84.43	21.84	26.05	36.49	111.95	36.00	63.87	18.72	3.30	

1) Granodiorite

The granodiorite is slightly siliceous (65.03 - 68.94 wt% SiO_2) and potassic (2.04 - 2.63 wt% K_2O). It exhibits high contents of Fe_2O_3 (2.9 - 4.18 wt%), MgO (1.52 - 2.19 wt%), and Na_2O (4.41 - 5.1 wt%). The petrographic nature of the samples is confirmed as granodiorite in the SiO_2 – Na_2O + K_2O diagram of [30] (**Figure 9(a)**), but sample PC0334 is similar to a trondhjemite in the classification (An-Ab-Or) of [31] (**Figure 9(b)**). The granodiorite is metaluminous (A/CNK < 1) (**Figure 9(c)**) [32] and belongs to the calc-alkaline magmatic series (**Figure 9(d)**) [33]. This rock is characterized by a sum of ΣREE ranging from 136.21 to 138.7 ppm. It is more enriched in LREE than in HREE, with (La/Yb)N and (La/Sm)N ratios ranging from 29.36 to 32.67 and from 4.1 to 4.3, respectively. The typical granodiorite facies shows a low fractionation rate marked by an Eu anomaly (Eu/Eu* = 0.91), while the trondhjemite facies shows a positive Eu anomaly (Eu/Eu* = 1.3) (**Figure 10(a)**). The multi-element spectrum normalized to the primitive mantle of [34] (**Figure 10(b)**) shows negative anomalies in Cs, Ba, Nb, Ta, Ce, Pr, P, Zr, Ti, Yb, and Lu, and positive anomalies that are sometimes very pronounced in Rb, U, La, Pb, and Sr.

2) Medium-grained biotite granite

Two medium-grained biotite granite samples were selected. They have an SiO_2 content of 69.32 wt% and an average normative quartz (CIPW norm) of 24.24% (**Table 6**). They contain high contents of Fe_2O_3 (2.81 - 2.90 wt%) and MgO (0.8 - 1.11 wt%) (**Table 6**). Alkalis (Na_2O + K_2O) range from 7.09 to 7.14 wt%. The trace chemical composition of significant incompatible elements shows low Th (10.70 - 13.90 ppm) and U (2.80 - 4.90 ppm), with a Th/U ratio ranging from 2.18 to 4.96, close to the mean crust value (Th/U = 4) (**Figure 11**). The sum of the rare earth elements (ΣREE) ranges from 198.9 to 321.82 ppm (**Table 7**). The rare earth spectra normalized to the primitive mantle show an enrichment in light rare earth elements (LREE) and a depletion in heavy rare earth elements (HREE). This granite displays relatively high fractionation, with (La/Yb)N ranging from 46.77 to 84.43 and a negative Eu anomaly (Eu/Eu* = 0.78 - 1.08) (**Figure 10(a)**). It is enriched in incompatible elements (Cs, Rb, U, Pb, La), with negative anomalies in Nb, Ta, Ce, Sr, P, Ti, and Tm (**Figure 10(b)**). These samples plot in the granite field of the SiO_2 – Na_2O + K_2O diagram of [30] and the An-Ab-Or diagram of [31] (**Figure 9(a)** and **Figure 9(b)**). This granite has a metaluminous character (A/CNK = 0.8 - 1.0) and a strongly potassic calc-alkaline composition (**Figure 9(d)**). One of the two samples

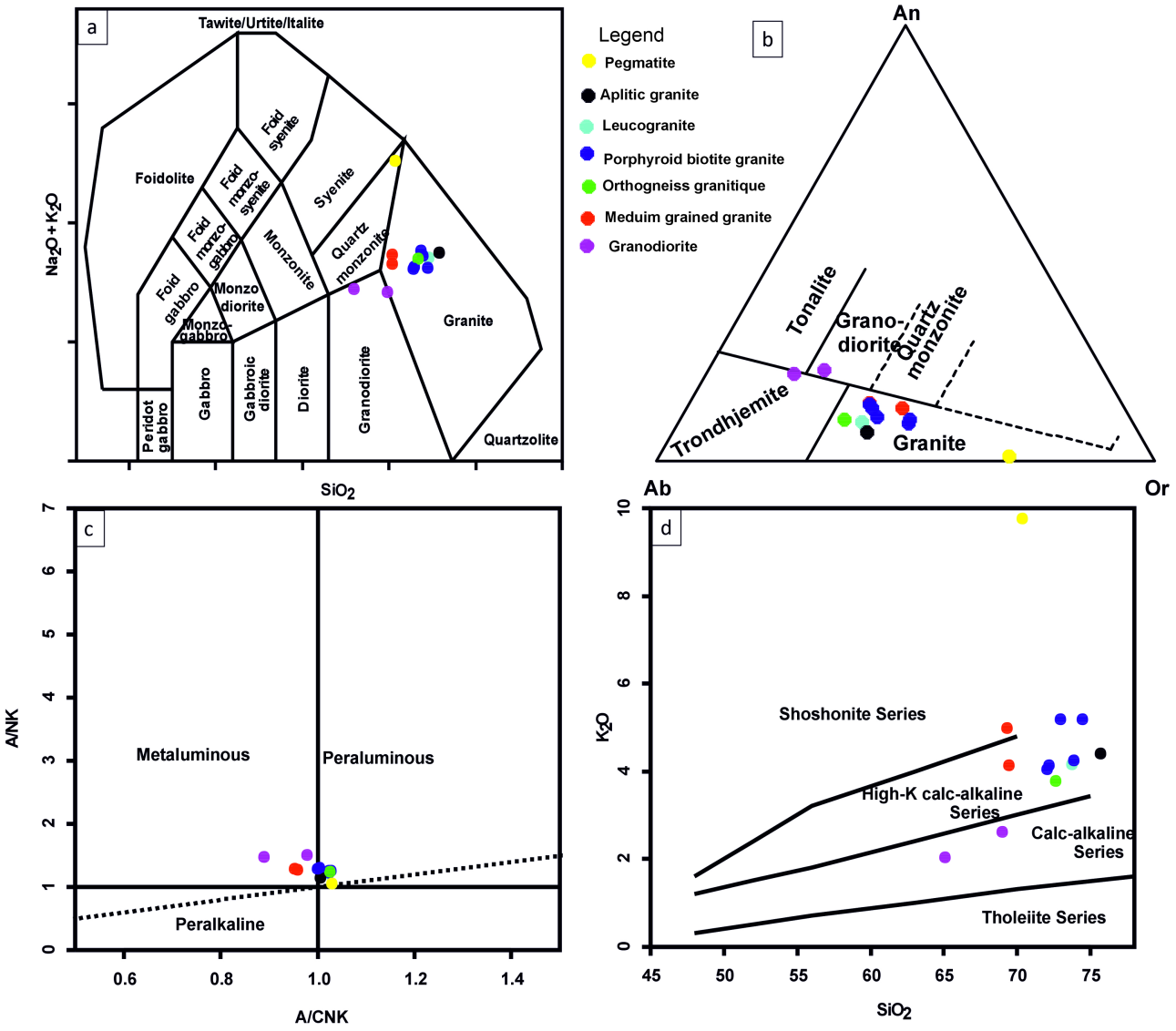

Figure 9. Classification and geochemical affinities of the Kindi granitoids. (a) (K_2O + Na_2O) vs. SiO_2 diagram of [30]; (b) An-Ab-Or ternary diagram of [31]; (c) geochemical affinities in the (A/NK-A/CNK) diagram of [32]; (d) SiO_2 vs. K_2O diagram of [33].

shows a shoshonitic affinity.

3) Porphyroid biotite granite

Five representative and non-altered samples of the porphyroid biotite granite were analyzed to determine its geochemical composition. This granite is enriched in silica, with normative quartz ranging between 28.65 and 31.83 % (**Table 6**). Its major-element chemical composition ranges from 8.02 to 8.77 wt% of alkali elements (Na_2O + K_2O); 13.75 to 14.26 wt% of Al_2O_3; 1.27 - 1.83 wt% of CaO; 1.35 - 1.98 wt% of Fe_2O_3; and 0.33 - 0.67 wt% of MgO. The trace chemical composition of significant incompatible elements displays low to moderate Th (8.10 - 12.7 wt%) and U (0.8 - 6.1 ppm) with a low to high Th/U ratio of 2.1 - 10.6, suggesting that part of the U may have been leached and remobilized out of the granite [35] (**Figure 11**), and relatively low Ta, Nb, and Y concentrations (**Table 7**). The ΣREE

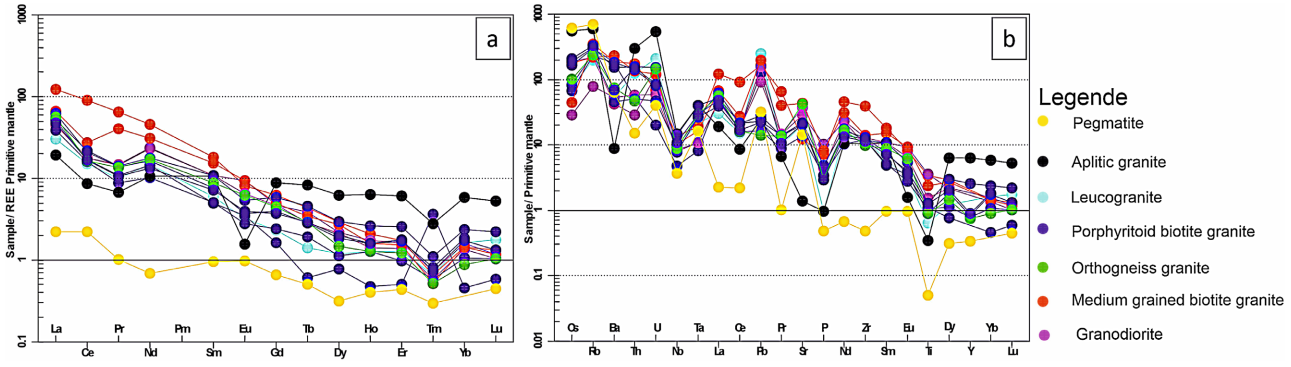

Figure 10. (a) Primitive mantle-normalized REE patterns of porphyroid biotite granite in the Kindi area [34]; (b) multi-element diagram normalized to the primitive mantle of [34].

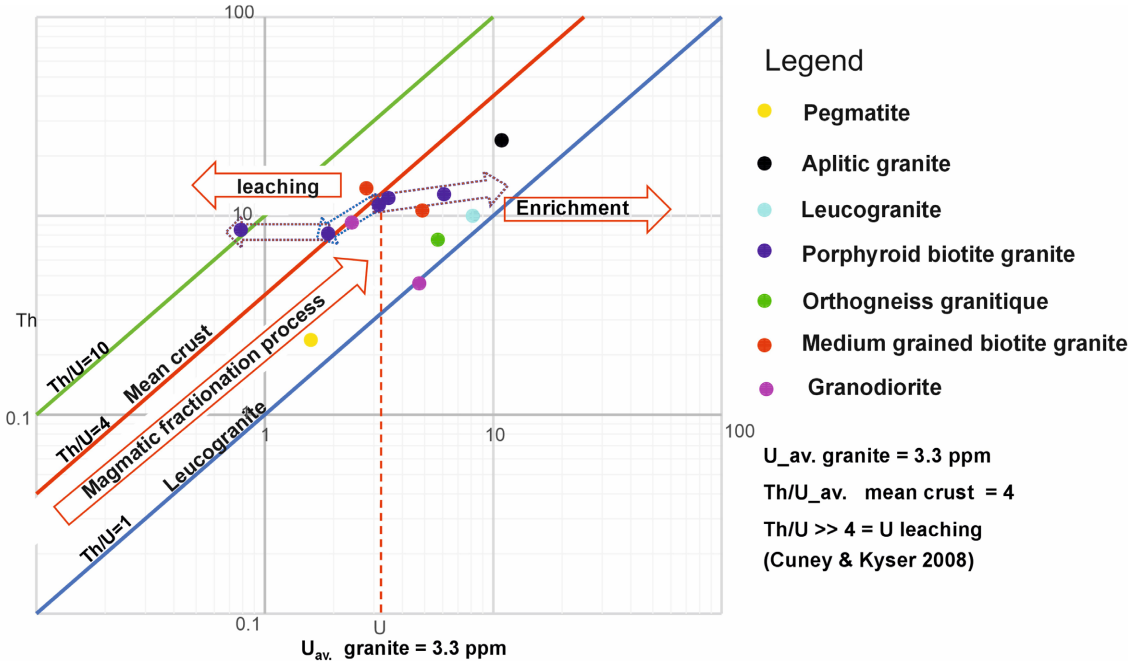

Figure 11. Log (U)-Log (Th) diagram from [35] showing the evolution of U, Th, and Th/U during magmatic fractionation in the Kindi granites.

ranges from 102.1 to 149.9 ppm. The REE spectra normalized to the primitive mantle of [34] (**Figure 10(a)**) exhibit strong enrichment in light rare earth elements (LREE) relative to heavy rare earth elements (HREE) (46.77 < (La/Yb)N < 111.95) and a weakly to moderately fractionated pattern, highlighted by a slight negative Eu anomaly (Eu/Eu* = 0.68 - 0.80), which likely characterizes the fractionation of plagioclase, except for one sample that shows a tendency towards accumulation (Eu/Eu* = 1.24). The multi-element diagram (**Figure 10(b)**) also shows negative anomalies in Ba, Nb, Ta, Ce, P, Ti, Y, Pr, and Tm and enrichment in Cs, Rb, Sr, U, and Pb, except for sample PC0457A, which may have experienced post-crystallization alteration (Th/U > 10). The granitic composition of the porphyroid biotite granite is confirmed by the (K_2O + Na_2O) vs SiO_2 diagram of [30] and further corroborated by the An-Ab-Or diagram of [31] (**Figure 9(a)** & **Figure**

9(b)). Therefore, this porphyroid biotite granite is metaluminous to slightly peraluminous (1.0 < A/CNK < 1.2; Figure 9(c); [32]) and belongs to a moderately fractionated high-K calc-alkaline to shoshonitic magmatic series (4.06 < K_2O < 5.21 wt%; Figure 9(d); [33]), corresponding with an A2-type granite affinity [36].

4) Augen granitic orthogneiss

Augen granitic orthogneiss has a very similar geochemical signature compared with the porphyroid biotite granite. Their respective REE spectra are concordant, and the cumulative REE (ΣREE) is 128.54 ppm. These spectra show an enrichment in LREEs of around 5 to 60 times the content of the primitive mantle, with (La/Sm)N = 6.39 and (La/Yb)N = 63.87. It shows a low fractionation rate marked by a very slight Eu anomaly (Eu/Eu* = 0.98). There is an enrichment in incompatible elements (U, Rb, Sr, La) and a series of significant negative anomalies in Th, Nb, P, Ti, Y, Ce, and Pr.

5) Leucogranite

The leucogranite sample displays a granite composition within standard classification diagrams (Figure 9(a), Figure 9(b)). The major and trace element composition is similar to that of porphyroid biotite granite. It is characterized by relatively low contents of MgO (0.16 wt%), Fe_2O_3 (1.05 wt%), and CaO (1.26 wt%) and high contents of Na_2O (4.31 wt%), K_2O (4.16 wt%), and U (8.3 ppm) (Table 6 and Table 7). The total sum of rare earth elements (ΣREE) is 100.29 ppm (Table 7). The REE spectra indicate an enrichment in light rare earth elements ranging from 5 to 60 times the content of REE in the primitive mantle as reported by [34]. They have an overall depletion in heavy rare earth elements (HREE). The degree of fractionation is moderate, with (La/Sm)N = 5.17, (La/Yb)N = 18.72, and a negative anomaly in Eu (Eu/Eu* = 0.87). The multi-element spectrum reveals a series of negative anomalies in Th, Nb, P, Ti, and Y, and positive anomalies in Rb, U, La, Sr, Nd, and Dy.

6) Dyke and vein systems

The vein facies, represented by aplitic granite and pegmatite, both have the composition of granite in the two classification diagrams used. Their major and trace-element contents approximate those of porphyroid biotite granite, with some slight variations.

Aplitic granite is more siliceous (75.66 wt% SiO_2) and slightly richer in alkalis, with 8.75 wt% Na_2O + K_2O. It has remarkable contents of Th (24 ppm) and U (10.9 ppm). However, it has low contents of Al_2O_3 (13.65 wt%), Fe_2O_3 (0.85 wt%), MgO (0.08 wt%), and CaO (0.92 wt%). The aplitic granite differs in that the REE spectrum is consistent with that of the primitive mantle [34]. It shows a sum of REE (ΣREE) = 79.25 ppm, ratios of (La/Sm)N = 3.3 and (La/Yb)N = 1.5, a well-pronounced negative Eu anomaly (Eu/Eu* = 0.16), negative anomalies of Ba, Nb, Ce, Pr, Sr, P, and Ti, and positive anomalies of Rb, Th, U, Ta, La, and Pb.

The pegmatite stands for its low content of SiO_2 (70.32 wt%), Fe_2O_3 (0.45 wt%), MgO (0.05 wt%), CaO (0.19 wt%), Th (2.4 ppm), U (1.6 ppm), and Zr (5 ppm). However, it has a high content of alkalis (Na_2O+K_2O) (12.57 wt%) and Al_2O_3

(15.94 wt%), and shows a REE spectrum similar to that of the primitive mantle. The sum of the REE (ΣREE) is 10.3 ppm, and the ratio (La/Sm)N is 4.66, with a positive Eu anomaly (Eu/Eu* = 1.22). The multi-element spectrum normalized to the primitive mantle of [34] shows a sawtooth pattern with more or less negative anomalies in Zr, P, Ti, and Y, and positive anomalies in Cs, Rb, U, Ta, Pb, and Sr.

5. Discussion

5.1. Geotectonic Context of the Kindi Granitoid Emplacement

The granitoids in the study area are associated with a volcanic arc context on the Yb-Ta diagrams of [37] (**Figure 12(a)**). In addition to the pegmatite and, to a lesser extent, the aplitic granite (Th/Ta = 16 and La/Nb = 1.30), the orogenic signature marked by values of Th/Ta > 5 and La/Nb > 2.5 [38] [39] for all the granites is also confirmed. The less fractionated terms represented by granodiorite and trondhjemite belong to a pre-collisional domain in the R1 - R2 diagram of [40] (**Figure 12(b)**). The medium-grained biotite granite may have been emplaced in a late-orogenic setting, while the porphyroid biotite granite, granitic orthogneiss, and leucogranite are late orogenic to syncollisional, and the aplitic granite and pegmatite were likely emplaced in a post-orogenic to anorogenic context according to the same diagram.

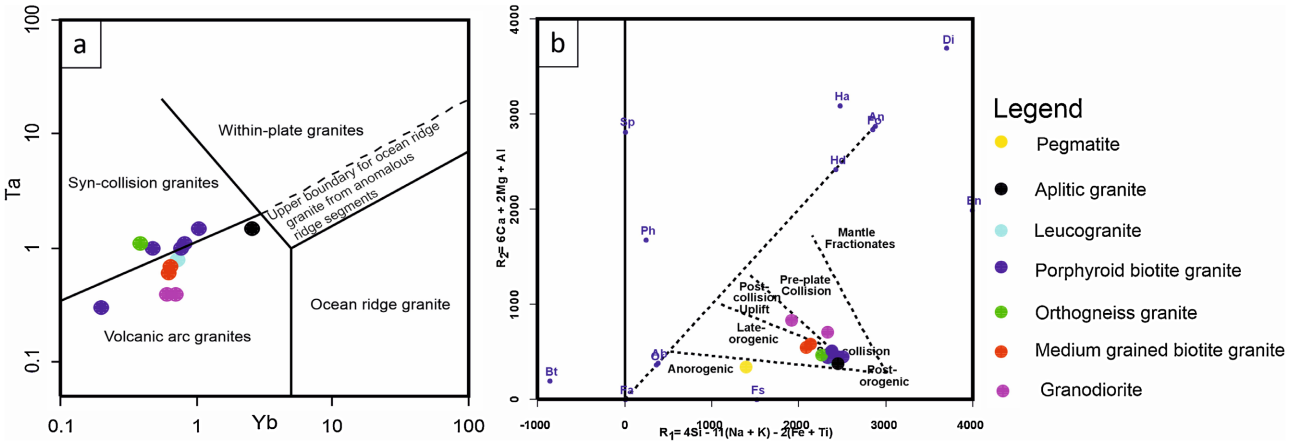

Figure 12. Geotectonic affinities of the Kindi granites in the diagrams (a) Yb-Ta by [37] and (b) R1-R2 by [40].

5.2. Petrogeochemical Characteristics

In the Kindi anomalous area, the studied igneous rocks present signatures of volcanic-arc to syncollisional granitoids (**Figure 12(a)**) and can be defined as calc-alkaline-potassic A2-type granite according to the Villasseca A-B chemico-mineralogical diagram, modified by [18] (**Figure 13(a)**). These rocks consist of two massifs corresponding to two distinct suites.

The first group is represented by medium-grained biotite granite. This rock is a metaluminous, high-K, calc-alkaline to shoshonitic granite, typical of the fractionated terms from the enriched mantle of [41] (**Figure 13(b)**).

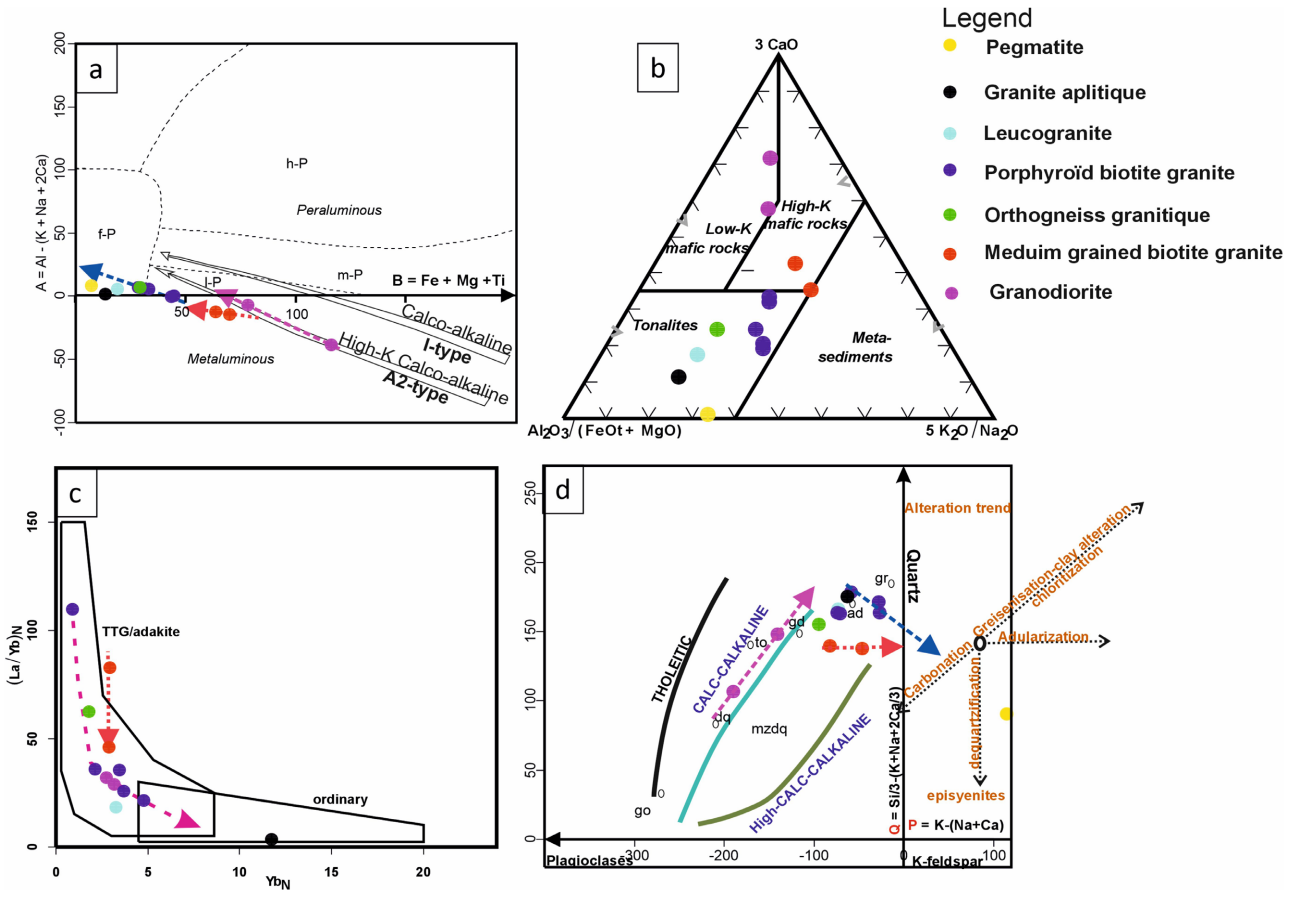

Figure 13. Geochemical affinity of the Kindi granites. (a) In the chemico-mineralogical A-B diagrams of Villasseca, modified by [18]; (b) 3CaO-5K_2O/Na_2O-Al_2O_3 by [41]; (c) (La/Yb)n vs (Y)n diagram of [42]; (d) P-Q of Debon and Lefort (1988), modified by [18].

The second group is represented by the porphyroid biotite granite massif. Together with trondhjemite, granodiorite, augen granitic orthogneiss, leucogranite, and aplitic granite, they form a suite that seems like the TTG/Adakites of [42] (**Figure 13(c)**) fractionated or partially melted [41] (**Figure 13(b)**) to adamelites (**Figure 13(d)**). The less fractionated terms in this group have a metaluminous and calc-alkaline composition. They are similar to granites derived from fractionation of the depleted mantle (**Figure 13(b)**).

The medium-grained biotite granite group is represented by syn- to late-orogenic terms dated between 2143 ± 4 Ma and 2150 Ma by [21], with signatures of Eu/Eu* = 0.78 - 1.08 and ΣREE = 198.9 - 321.82 ppm, reflecting plagioclase fractionation. This facies is relatively rich in ferromagnesian, accessory, and secondary minerals, mainly represented by ferriferous biotite frequently altered to muscovite and chlorite; metamorphic sphene; zoned allanite, apatite, damourite, calcite, pistachite-type epidote, and haematite. This granite is depleted in the trace elements Sr, Nb, Ta, Ce, P, Ti, Tm ± Pr, and enriched in incompatible elements such as Cs, Rb, U, Pb, and La.

The second massif, represented by late-orogenic to syn-collisional porphyroid biotite granite, is younger, at around 2110 ± 8 Ma to 2099 ± 10 Ma, according to

the same author. It is the major facies of the second potassic calc-alkaline sub-series of type A2 of Villasseca's A-B chemico-mineralogical diagram, modified after [18]. Fairly peraluminous to peraluminous, it is more fractionated (Eu/Eu* = 0.68 - 1.24 and ΣREE between 100.29 and 149.9 ppm) than the medium-grained biotite granite. Both granites contain very similar mineral assemblages. However, the proportions of ferromagnesian, accessory, and secondary minerals are lower in the porphyroid biotite granite, although an apparent enrichment in ankerite-type carbonate, zircon, and apatite is observed. These mineralogical associations are supported by chemical signatures marked by a depletion in Ba, Y, Nb, Ta, Ce, P, Ti, Tm, and Pr and an enrichment in Sr, Cs, Rb, U, and Pb. The early terms of the series, represented here by the granodiorite and the pre-collisional trondhjemite (**Figure 8(a)**), are less fractionated, with Eu/Eu = 0.91 - 1.3 and ΣREE between 136.21 and 138.7 ppm. They are less siliceous, less potassic, and depleted in Ba, Cs, Zr, Nb, Ta, Ce, Pr, P, Ti, Yb, and Lu. They are, however, enriched in Na-Sr-Rb-U-Pb-La.

5.3. Deformation of Granitoids

The Kindi anomaly is overlaid on a porphyroid biotite granite intruded into a medium-grained biotite granite along a northeast (N50˚E) trending sinistral shear zone. This shear zone corresponds to one of the relay structures of the N-S-oriented Wa-Laura-Jirapa translithospheric shear [6] [21], which, at the scale of the Koudougou sheet, defines a system of large sinistral shears marked by the verticalization of the volcano-sedimentary strata and the rotation of the structural directions associated with variably oriented planar structures represented by sub-vertically dipping schistosity, varying in strike direction from N5˚ to N40˚E in the south and from N70˚E to N90˚E in the northeast of the map sheet where the Kindi anomaly is located.

This N50E corridor affecting the Kindi anomaly is highlighted by a granitic orthogneiss with a protomylonite structure superimposed by brittle deformation. It is characterized by the presence of almond-shaped feldspars and ribbons of orthoclase and microcline.

The porphyroid biotite granite bordering the N50E corridor has a fusiform appearance and a deformed edge marked by a very clear planar orientation of the feldspars. These feldspars, sometimes zoned, are sigmoidal in shape as a result of shearing deformation. It is also cut by bands of syn-collisional leucogranite and post-orogenic aplitic granite, both affected by cataclastic and mylonitic deformation, as well as by veins of anorogenic pegmatite, sometimes individualised in the form of puffs with pegmatitic megacrysts.

The medium-grained biotite granite is affected by a large network of fractures and by relatively more cataclastic deformation, which locally lead to zones of intense fracturing marked by numerous diaclases, often injected with pegmatite and quartz veinlets.

5.4. Hydrothermal Alteration

The lithostructural context defined in the Kindi area is associated with hydrother-

mal alteration. Supported by mineralogical assemblage descriptions, many types of hydrothermal alteration have been pointed out through secondary mineral studies. Discrimination of biotite in the Kindi granites, based on the ternary diagram of [25], shows that they are essentially derived from a re-equilibrated environment in which subsequent hydrothermal fluids were involved in their formation (**Figure 3(d)**).

The less fractionated terms, such as granodiorite and trondhjemite, in the series display sodium propylitic alteration, illustrated by chlorite-epidote-calcite-Fe-oxide assemblages filling a dense network of microfractures. This rock is characterised by a depletion in Cs, Sr, and Yb, and an enrichment in CaO and Na_2O, as well as in the incompatible elements Rb (95.6 to 131.2 ppm), U (2.4 to 4.8 ppm), Pb (13.86 to 23.91 ppm), and Yb (0.6 to 0.7 ppm), and trends toward carbonatation alteration in the modified diagram of Debon and LeFort [18] (**Figure 13(b)**).

The medium-grained biotite granite displays greisenization and potassic alteration mineral assemblages. It contains abundant phases of microperthitic and poecilitic microcline and orthoclase, often altered into muscovite (**Figure 7(a)**) and are frequently fractured with infilling of secondary quartz. The perthitisation of the phases is very often associated with tectonics and/or fluid circulation [43] resulting from dequartzification combined with the loss of volatile substances from the system, which enriched it in silica, carbonate and hematite [44]. This alteration sometimes involves the digestion of certain portions of the large patches of these feldspars and biotite (**Figure 7(b)**), as well as the filling of cracks in the potassic feldspars by crystallization of secondary brown biotite, which sometimes replaces the chloritized biotite, according to petrographic observations. The geochemical data revealed a depletion in Sr (865.8 to 246.4 ppm) and an enrichment in Ba (1522 to 1232 ppm), Cs (7.5 to 1.9 ppm), Rb (211.8 to 132.4 ppm), U (4.9 to 2.8 ppm), and Pb (29.6 to 24.9 ppm). The signature of a potential hydrothermal alteration by adularisation defined by the modified P-Q diagram of Debon and Lefort [18] (**Figure 13(b)**), which corresponds to potassic alteration by the circulation of hot fluids under pressure rich in dissolved elements [45], corroborates the previous observations.

The major constituents of the porphyroid biotite granite show phase exsolution, probably associated with an increase in volatile elements [46] [47]. This exsolution is materialised, on the one hand, by the myrmekitisation of plagioclases observed in thin sections (**Figure 8(b)**) and their alteration into sericite-ankerite-calcite-quartz, and, on the other hand, by the destabilisation of biotites into chlorite-epidote-hematite-muscovite. Some of these altered minerals are overlain by poecilitic potassic feldspars, characteristic of the evolution of a residual alkaline-rich fluid phase from an almost consolidated igneous body defined by [48]. Stress alteration is probably associated with the circulation of hot potassic oxidising fluids (presence of haematite) carried to the chlorite-epidote isograde (temperature > 300 ˚C) [49] and highlighted by a depletion in Ba (1216 to 608 ppm), ±in Y, and an enrichment in Sr (852.4 to 270 ppm), Cs (12.8 to 2.8 ppm), Rb (415.7 to 117.8 ppm),

U (8.3 to 0.8 ppm), Pb (18.54 to 4.2 ppm), La (40.2 to 2.9 ppm), Dy (2 to 0.21 ppm), and Yb (1.05 to 0.18 ppm). The depletion or enrichment of these chemical elements beyond the magmatic fractionation process is essentially linked to mineralogical and geochemical changes that occur during the fluid/rock alteration process [50]. The paragenesis described corresponds to potassic and propyllitic alteration, overlain by the episyenitisation-type signature of the modified P-Q diagram of [18] (**Figure 13(b)**), characterised by carbonation and silicification, probably linked to the circulation of potassium-rich fluids. The leucogranite, depleted in Zr, P, Ti, and Y and enriched in Sr (402.6 ppm), Cs (3.30 ppm), Rb (117.8 ppm), U (8.3 ppm), Ta (0.8 ppm) and Pb (37.5 ppm), and the aplitic granite, depleted in Ba-Sr-P-Ti and enriched in U (10.9 ppm), Ta (1.5 ppm), Pb (7.4 ppm) and La (12.5 ppm), which represent the more advanced terms in this series, are both affected by potassic and propyllitic alteration.

Pegmatite is a late-crystallisation or hydrothermal-transition facies, rich in K-feldspars and secondary muscovite, very often associated with potassic metasomatism [51] [52]. It is intruded into porphyroid granite and emplaced along a shear corridor, a structural pathway that facilitated the ascent of magma and the circulation of hydrothermal fluids [53]. Its emplacement in the system likely contributed to providing magmatically derived fluids and their induced hydrothermal alteration of the host rocks.

5.5. Lithological Fertility

The petrogeochemical characteristics show that granitoids of the Kindi anomaly, which extend to the other anomalies in the Koudougou region, have potential for granite-related hydrothermal uranium mineralisation, such as that defined by [29] and [54] in the Nanling metallogenic belt in southern China.

The pre-orogenic granodiorite/trondhjemite facies is not considered a potential fertile source of uranium for a granite-related hydrothermal system, as it represents a poorly differentiated granitoid of low-K calc-alkaline affinity and poorly enriched in U, as shown by sample JM0372 (U = 2.4 ppm; Th/U = 3.9), even though it may host post-magmatic hydrothermal U concentrations in altered zones characterized by propylitic alteration, as shown in sample PC0334 (U = 4.8 ppm; Th/U = 0.9).

The medium-grained biotite granite of the Kindi anomaly has U contents of 2.8 to 4.9 ppm and a Th/U ratio between 2.2 and 4.9 (**Figure 11**). This late-orogenic granite, rich in biotite and metamorphosed accessory minerals, is fractured and affected by potassic hydrothermal alteration, as demonstrated by the dissolution of magmatic K-feldspar and the precipitation of secondary muscovite and quartz, suggesting greisenization of this granitic pluton. Sample PC0335A may have been slightly enriched in U (4.9 ppm) during late- to post-magmatic hydrothermal alteration, as shown by a Th/U of 2.2, while the U content of 2.8 ppm in sample PC0343 likely reflects the primary magmatic U concentration in the medium-grained biotite granite characterized by a Th/U value of 4.9, which is close to the

mean crustal value (*i.e.*, Th/U = 4). Although the medium-grained biotite granite contains potentially U-bearing accessory minerals such as sphene and allanite that may have released part of their U contents, supported by the observation of metamictization textures, this granitoid would, however, hardly provide a significant amount of U to a potential hydrothermal system due to its relatively low magmatic U concentration (*i.e.*, ~3 ppm).

In contrast, the syn- to late orogenic porphyroid biotite granite, although presenting a similar major and accessory mineral assemblage to the medium-grained biotite granite, is a more fractionated granite with peraluminous high-K calc-alkaline to shoshonitic affinity and a much lower ferromagnesian mineral content, also characterized by a continuous enrichment of U and Th during magmatic fractionation (**Figure 11**). It is intruded within less evolved lithofacies (e.g., granodiorite, throndhjemite) of the Kindi anomaly, along a NE-SW shear corridor, and is affected by late- to post-magmatic potassic and propylitic hydrothermal alteration characterized by secondary mineral assemblages of muscovite-quartz and chlorite-epidote-carbonate, respectively. Its variable U content, ranging from 0.8 to 6.1 ppm, is likely hosted by accessory minerals such as allanite and sphene, both showing characteristic destruction halos of metamictization texture, indicating that part of their U content has been released into the rock. While sample PI15 may reflect the initial U concentration within this granite (U = 3.4 ppm; Th/U = 3.6), Th/U values up to 10.6 in sample PC0457A, associated with U depletion down to 0.8 ppm, indicate that part of its U content has been leached by fluids in altered zones, which may have been transported and trapped along fractures, faults, and shear zones. Slight U enrichment (U = 5.8 ppm; Th/U = 1.3) in gneissified parts of the porphyroid biotite granite (e.g., orthogneiss sample PI07B) tends to corroborate this hypothesis and thus could validate the local potential for granite-related hydrothermal mineralization.

In addition, the Villy anomaly, located some twenty km from the Kindi anomaly, is confined to a medium-grained biotite granite hosting a migmatitic biotite leucogranite with a cataclastic texture, which lies along the axis of the shear corridor. It is cut by a younger dolerite dyke, probably of Mesoproterozoic age. The emplacement of these dykes is generally accompanied by the circulation of magmatically derived hydrothermal fluids. The dyke-leucogranite-medium-grained granite-biotite intersection would constitute an additional enrichment factor likely to facilitate the concentration of uranium, following the example of the work by [55] and [56] in the Xiazhuang mining district in southern China.

Finally, late intrusions of 2-micas leucogranite and granitic aplite, which cross-cut both the medium-grained and porphyroid biotite granites, present moderately to strongly fractionated peraluminous signatures and have the highest primary U concentrations within the Kindi anomalous area, at 8.3 ppm and 10.9 ppm, respectively, with Th/U values of 1.2 and 2.2, which are consistent with the leucogranite geochemical signature (**Figure 11**). It should be noted that granitic aplites are often associated with pegmatite veins and have a similar mineral compo-

sition to that of the porphyroid biotite granite, and thus could represent a late, highly fractionated term of this granitic magma.

Therefore, the porphyroid biotite granite, and more particularly the granitic aplite and leucogranite within the Kindi anomalous area, showed significant U concentrations that could characterize them as fertile source rocks, and textural evidence for U release from U-bearing accessory minerals, as well as footprints of U remobilization and local enrichment in structural corridors affected by late-to post-magmatic hydrothermal alteration, which could define this area as prospective for granite-related U mineralization.

Several generations of potassic calc-alkaline granites similar to the granites of the Kindi anomaly have produced vein-type uranium deposits associated with these granites. This is the case for the Maofeng pluton in the Nanling metallogenic belt [29] in southern China, which is reputed to be fertile and hosts several deposits of uranium and rare and precious minerals. This pluton is composed of biotite granites, medium- and coarse-grained two-mica granites, and leucogranite [57] [58]. The granites of this pluton contain mainly biotite, muscovite, quartz, and alkali and calcic feldspars, and secondarily minerals such as adularia, epidote, fluorapatite, titanite, and various sulphides. Unlike the Kindi granites, they have U contents very often > 10 ppm and marked evidence of alteration corridors along extensive post-orogenic structures that are not clearly identified in the Kindi zone. In north-west China, in the Baiyanghe deposit, the same type of biotite granite, associated with the Yangzhuang pluton, has been defined as a secondary source of U mobilised along fractures after the rhyolitic tuffs, which constitute the primary source. Like the medium-grained biotite granite at Kindi, this granite has U contents of between 2.3 and 4.3 ppm (mean U content = 2.9 ppm) and a Th/U ratio close to the average content of the continental crust (2.4 to 6.1) [59]. It shows a release and remobilisation of U from accessory minerals containing U in a metamict state.

The most fractionated terms of the Maofeng pluton, represented by the leucogranite, are excellent fertile sources for hydrothermal U mineralisation [57] [58], as are the uraninite-bearing leucogranites of the French Massif Central [60]. These facies, associated with the biotite granite at Maofeng, are highly enriched in U, with concentrations ranging from 11.1 to 32.7 ppm and a Th/U ratio ranging from 0.4 to 2.0.

Further investigation of the medium-grained biotite granite massif at Kindi could reveal similar leucogranites, which would correspond to the evolved terms of the suite for which the least-differentiated terms described have the same characteristics.

At Saraya, in south-eastern Senegal, in the Kédougou-Kéniéba buttonhole, Paleoproterozoic (~2079 Ma) peraluminous two-mica leucogranites associated with a granitic complex host metasomatic uranium mineralisation affected by albitisation and episyenitisation processes. This major sodic metasomatic event associated with uranium mineralisation has been documented in the Palaeoprote-

rozoic and Mesoproterozoic [20].

In the Reguibat Shield, Mauritania, Palaeoproterozoic granitoids similar to the Kindi biotite porphyritic granite massifs were good reservoirs for the mobilisation of hydrothermal uranium under oxidising and evaporitic conditions at the surface to supply large second calcrete-type U deposits [19]. The granite formations that host this mineralisation are peraluminous, calc-alkaline to shoshonitic granites composed of a porphyritic pink granite with a mylonitic texture, syncollisional, weakly evolved, and a more evolved grey granite with a massive to locally oriented medium grain, postorogenic. The pink granite has U contents > 17 ppm and Th/U ratios of 0.4 to 2.0, and U contents (≈13 - 16 ppm) for the grey granite and Th/U ratios ≤ 1.5. The postorogenic Kindi aplitic granite with 10.9 ppm U and a Th/U ratio of 2.2, also described locally as a grey granite, is similar in every respect to the grey granite of Mauritania.

U-fertile facies have now been identified in the Kindi zone, but it remains to be seen whether these facies are sufficient to generate economic mineralisation. Further investigation will enable us to carry out an in-depth characterisation to better assess the zone's uranium potential.

6. Conclusions

The granitoid fertility assessment as a potential source rock for granite-related hydrothermal uranium mineralisation focused on the petro-geochemical characterisation of the main granitic facies from the Kindi radiometric anomalous area and helped to define the major geological context of these anomalies in Burkina Faso. The main granitoids that were studied in the Kindi area include TTG (Tonalites-Trondhjemite-Granodiorites) and medium-grained biotite granite, which were intruded by porphyroid biotite granite, leucogranite, and aplo-pegmatitic dykes in this region.

Early Birrimian TTG are poorly fractionated, rich in biotite and amphibole, and present a metaluminous, calc-alkaline magmatic affinity. They are enriched in Na, Ca, Fe, and Mg but display low K, U, and Th concentrations. Although they exhibit post-magmatic hydrothermal U concentrations locally in altered zones characterized by propylitic alteration, they are not considered a potential fertile source of uranium for a granite-related hydrothermal system.

Similarly, the medium-grained biotite granite represents metaluminous, potassic calc-alkaline terms of late-orogenic granite, rich in biotite and uraniferous accessory minerals and enriched in Cs-Rb-U-Pb-REE. It is cataclased and affected by potassic hydrothermal alteration and greisenization. This type of granite has a low magmatic U concentration and could provide minor amounts of U to a potential hydrothermal system.

In contrast, fertile sources of uranium for a granite-related hydrothermal system in the Kindi area would correspond to the porphyroid biotite granite, its gneissified parts, the leucogranite, and the associated network of aplo-pegmatitic dykes. They belong to weakly peraluminous, high-K calc-alkaline to shoshonitic

magmatic series emplaced during syn- to late-orogenic and post-orogenic periods. They are less rich in biotite but present a similar uraniferous accessory mineral assemblage to the medium-grained biotite granite. They are characterised by low Na-Ca, Fe, and Mg contents but higher concentrations of incompatible elements such as K (up to 5.21 wt% oxide), U (up to 6.10 ppm), and Th (up to 12.70 ppm). The porphyroid biotite granite is affected by a shear corridor highlighted by potassic and propylitic hydrothermal alterations. Metamictization texture, characterised by destruction halos surrounding uraniferous accessory minerals (allanite and sphene), indicates that part of their U content has been released into the rock. This U may then have been leached by oxidizing fluids and remobilized along structural corridors affected by late- to post-magmatic hydrothermal alteration to potentially form uranium mineralisation. Similar contexts have been documented as favourable for granite-related hydrothermal uranium mineralisation, extended to rare and precious metal mineralisation, in other parts of the West African Craton, such as in the Saraya Batholith in Senegal and in the Regibat Shield in Mauritania. Therefore, the fracturing and alteration zones affecting these fertile granitic rocks should be mapped in detail to further identify favourable targets for regional uranium exploration.

Conflicts of Interest

The authors declare no conflicts of interest regarding the publication of this paper.

References

[1] CEA (1958) Territoire de Haute Volta: Intérêt et programme d'une prospection pour métaux radioactif.

[2] Marchat, M.E. (1981) Upper Volta uranium exploration project. UTAH Development Company, Final Report Upper Volta. Report N351.

[3] CGG (1999) Rapport définitif sur l'interprétation des données des levés magnétométriques et radiométriques aériens de l'ouest du Burkina Faso. Programme SYSMIN (7ACP BK 074). Ministère de l'Energie et des Mines.

[4] Geotech Ltd (2016) Rapport Final: Acquisition et Traitement. Cartographie de Géophysique aéroportée en magnétisme et spectrométrie gamma sur le quart NE du Burkina Faso. Rapport produit par GEOTECH LTD dans le cadre du projet Padsem.

[5] Castaing, C., Billa, M., Milési, J.P., Thiéblemont, D., Le Métour, J., *et al.* (2003) Notice explicative de la carte géologique et minière du Burkina Faso à 1/1 000 000. BRGM, Orléans.

[6] Dahl, R., Hein, K.A.A., Séjourné, S., Ouedraogo, C., Giovenazzo, D., *et al.* (2018) Carte de synthèse géologique, structurale et des substances minérales du Burkina Faso à 1/1 000 000. Projet d'Appui au développement du Secteur minier (PADSEM). Ministère des Mines et des Carrières.

[7] Yaméogo, A.O., Ouiya, P., Traoré, A.S., Sawadogo, S., Naba, S., Rousse, S., *et al.* (2023) Rheological Context of Emplacement of the Dori, Gorom-Gorom and Touka Bayèl Granitic Plutons (Northeast Burkina Faso, West African Craton). *Journal of African Earth Sciences*, **208**, Article 105081. https://doi.org/10.1016/j.jafrearsci.2023.105081

[8] Kagambega, N. (2005) Typologie des granitoides paleoproterozoiques (Birimien) du Burkina Faso-Afrique de l'Ouest: Approche petrologique dans la region de Po. These, Universite Cheick Anta Diop de Dakar.

[9] Tapsoba, B., Lo, C., Jahn, B., Chung, S., Wenmenga, U. and Iizuka, Y. (2013) Chemical and Sr-Nd Isotopic Compositions and Zircon U-Pb Ages of the Birimian Granitoids from NE Burkina Faso, West African Craton: Implications on the Geodynamic Setting and Crustal Evolution. *Precambrian Research*, **224**, 364-396. https://doi.org/10.1016/j.precamres.2012.09.013

[10] Hein, K.A.A., Morel, V., Kagoné, O., Kiemde, F. and Mayes, K. (2004) Birimian Lithological Succession and Structural Evolution in the Goren Segment of the Boromogoren Greenstone Belt, Burkina Faso. *Journal of African Earth Sciences*, **39**, 1-23. https://doi.org/10.1016/j.jafrearsci.2004.05.003

[11] Naba, S., Vegas, N., Bouchez, J.L., Siqueira, R. and Lompo, M. (2006) Caractères magnétiques fabriques et contexte géodynamique des granites du Burkina Faso oriental: Les plutons de Tenkodogo-Yamba, de Kouare et de Naneni. *Africa Geoscience Review*, **13**, 63-76.

[12] Traore, A.S. (2011) Mise en place des plutons de granites alcalins Paléoprotérozoïques du Burkina Faso (Afrique de l'Ouest). Ph.D. Thesis, Université de Ouagadougou.

[13] Sawadogo, S., Naba, S., Ilboudo, H., Traoré, A.S., Nakolendoussé, S. and Lompo, M. (2018) The Belahourou Granite Pluton (Djibo Greenstone Belt, Burkina Faso): Emplacement Mechanism and Implication for Gold Mineralization along a Shear Zone. *Journal of African Earth Sciences*, **148**, 59-68. https://doi.org/10.1016/j.jafrearsci.2018.04.009

[14] Ilboudo, H., Sawadogo, S., Kagambega, N. and Remmal, T. (2021) Petrology, Geochemistry, and Source of the Emplacement Model of the Paleoproterozoic Tiébélé Granite Pluton, Burkina Faso (West-Africa): Contribution to Mineral Exploration. *International Journal of Earth Sciences*, **110**, 1753-1781. https://doi.org/10.1007/s00531-021-02039-3

[15] Bonzi, W.M., Vanderhaeghe, O., Van Lichtervelde, M., Wenmenga, U., André-Mayer, A., Salvi, S., *et al.* (2021) Petrogenetic Links between Rare Metal-Bearing Pegmatites and TTG Gneisses in the West African Craton: The Mangodara District of SW Burkina Faso. *Precambrian Research*, **364**, Article 106359. https://doi.org/10.1016/j.precamres.2021.106359

[16] Bonzi, W.M., Van Lichtervelde, M., Vanderhaeghe, O., André-Mayer, A., Salvi, S. and Wenmenga, U. (2022) Insights from Mineral Trace Chemistry on the Origin of NYF and Mixed LCT+NYF Pegmatites and Their Mineralization at Mangodara, SW Burkina Faso. *Mineralium Deposita*, **58**, 75-104. https://doi.org/10.1007/s00126-022-01127-x

[17] McCuaig, T.C., Beresford, S. and Hronsky, J. (2010) Translating the Mineral Systems Approach into an Effective Exploration Targeting System. *Ore Geology Reviews*, **38**, 128-138. https://doi.org/10.1016/j.oregeorev.2010.05.008

[18] Cuney, M. (2014) Felsic magmatism and uranium deposits. *Bulletin de la Société Géologique de France*, **185**, 75-92. https://doi.org/10.2113/gssgfbull.185.2.75

[19] Salem-Vall, B., Olatunji, A.S. and Hamoud, A. (2025) Geochemical and Mineralogical Characterization of Weathered Granite Hosting Secondary Uranium Mineralization: A Case Study from the Eastern Part of the Reguibat Shield, Northern Mauritania. *Journal of Geochemical Exploration*, **271**, Article 107698. https://doi.org/10.1016/j.gexplo.2025.107698

[20] Dieye, M., Faye, C.I., Diene, M., Cuney, M., Brouand, M. and Gueye, M. (2025) Uranium Mineralization Associated with Albitization in a Paleoproterozoic Granite: Ex-

ample of the Saraya Granite, (Eastern Senegal, West Africa). *Journal of African Earth Sciences*, **226**, Article 105570. https://doi.org/10.1016/j.jafrearsci.2025.105570

[21] Chevremont, P., Donzeau, M., Le Metour, J., Egal, E., Castaing, C., *et al.* (2003) Carte géologique du Burkina Faso à 1/200 000, Feuille Koudougou, BRGM, BUMIGEB, Ouagadougou.

[22] Foster, M.D. (1960) Interpretation of composition of trioctaheral micas. U.S. Geological Survey Professional Paper.

[23] Tulloch, A.J. (1979) Secondary Ca-Al Silicates as Low-Grade Alteration Products of Granitoid Biotite. *Contributions to Mineralogy and Petrology*, **69**, 105-117. https://doi.org/10.1007/bf00371854

[24] Nachit, H., Ibhi, A., Abia, E.H. and Ben Ohoud, M. (2005) Discrimination between Primary Magmatic Biotites, Reequilibrated Biotites and Neoformed Biotites. Comptes Rendus. *Géoscience*, **337**, 1415-1420. https://doi.org/10.1016/j.crte.2005.09.002

[25] Dunlop, D. and Ozdemir, O. (1997) Fundamental Frontiers; Cambridge Studies in Magnetism. Cambridge University Press.

[26] Trdlicka, Z. and Hoffman, V. (1976) Untersuchungen der chemischen Zusammensetzung der Gangkarbonate von Kutna Hora/CSSR. *Freiberger Forschungshefte*, **321**, 29-81.

[27] Bonnetti, C., Cuney, M., Bourlange, S., Deloule, E., Poujol, M., Liu, X., *et al.* (2017) Primary Uranium Sources for Sedimentary-Hosted Uranium Deposits in NE China: Insight from Basement Igneous Rocks of the Erlian Basin. *Mineralium Deposita*, **52**, 297-315. https://doi.org/10.1007/s00126-016-0661-0

[28] Bonnetti, C., Riegler, T., Liu, X. and Cuney, M. (2023) Granite-Related High-Temperature Hydrothermal Uranium Mineralisation: Evidence from the Alteration Fingerprint Associated with an Early Yanshanian Magmatic Event in the Nanling Belt, SE China. *Mineralium Deposita*, **58**, 427-460. https://doi.org/10.1007/s00126-022-01137-9

[29] Bonnetti, C., Liu, X.D., Mercadier, J., Cuney, M., Deloule, E., Villeneuve, J., *et al.* (2018) The Genesis of Granite-Related Hydrothermal Uranium Deposits in the Xiazhuang and Zhuguang Ore Fields, North Guangdong Province, SE China: Insights from Mineralogical, Trace Elements and U-Pb Isotopes Signatures of the U Mineralisation. *Ore Geology Reviews*, **92**, 588-612. https://doi.org/10.1016/j.oregeorev.2017.12.010

[30] Middlemost, E.A.K. (1994) Naming Materials in the Magma/Igneous Rock System. *Earth-Science Reviews*, **37**, 215-224. https://doi.org/10.1016/0012-8252(94)90029-9

[31] O'Connor, J.T. (1969) A Classification for Quartz-Rich Igneous Rocks Based on Feldspar Ratios. U.S. Geological Survey Professional Paper 525-B.

[32] Peccerillo, A. and Taylor, S.R. (1976) Geochemistry of Eocene Calc-Alkaline Volcanic Rocks from the Kastamonu Area, Northern Turkey. *Contributions to Mineralogy and Petrology*, **58**, 63-81. https://doi.org/10.1007/bf00384745

[33] Shand, S.J. (1943) Eruptive Rocks: Their Genesis, Composition, Classification, and Their Relation to Ore-Deposits, with a Chapter on Meteorites. Wiley.

[34] McDonough, W.F. and Sun, S. (1995) The Composition of the Earth. *Chemical Geology*, **120**, 223-253. https://doi.org/10.1016/0009-2541(94)00140-4

[35] Cuney, M. and Kyser, K. (2008) Recent and Not-So-Recent Developments in Uranium Deposits and Implications for Exploration. The Mining Association of Canada.

[36] Eby, G.N. (1992) Chemical Subdivision of the A-Type Granitoids: Petrogenetic and Tectonic Implications. *Geology*, **20**, 641-644.

https://doi.org/10.1130/0091-7613(1992)020<0641:csotat>2.3.co;2

[37] Pearce, J.A., Harris, N.B.W. and Tindle, A.G. (1984) Trace Element Discrimination Diagrams for the Tectonic Interpretation of Granitic Rocks. *Journal of Petrology*, **25**, 956-983. https://doi.org/10.1093/petrology/25.4.956

[38] Joron, J.L. and Treuil, M. (1977) Utilisation des proprietes des elements fortement hygromagmatophiles pour l'etude de la composition chimique et de l'heterogeneite du manteau. *Bulletin de la Société Géologique de France*, **7**, 1197-1205. https://doi.org/10.2113/gssgfbull.s7-xix.6.1197

[39] Gill, J.B. (1981) Orogenic Andesites and Plate Tectonics. Springer.

[40] Batchelor, R.A. and Bowden, P. (1985) Petrogenetic Interpretation of Granitoid Rock Series Using Multicationic Parameters. *Chemical Geology*, **48**, 43-55. https://doi.org/10.1016/0009-2541(85)90034-8

[41] Laurent, O., Martin, H., Moyen, J.F. and Doucelance, R. (2014) The Diversity and Evolution of Late-Archean Granitoids: Evidence for the Onset of "Modern-Style" Plate Tectonics between 3.0 and 2.5Ga. *Lithos*, **205**, 208-235. https://doi.org/10.1016/j.lithos.2014.06.012

[42] Martin, H. (1986) Effect of Steeper Archean Geothermal Gradient on Geochemistry of Subduction-Zone Magmas. *Geology*, **14**, 753-756. https://doi.org/10.1130/0091-7613(1986)14<753:eosagg>2.0.co;2

[43] Abart, R., Petrishcheva, E., Wirth, R. and Rhede, D. (2009) Exsolution by Spinodal Decomposition II: Perthite Formation during Slow Cooling of Anatexites from Ngorongoro, Tanzania. *American Journal of Science*, **309**, 450-475. https://doi.org/10.2475/06.2009.02

[44] Rout, D., Krishnamurthi, R. and Sinha, D.K. (2022) Mineralogy and Paragenesis of the Meso-Proterozoic Rohil Uranium Deposit, North Delhi Fold Belt, Rajasthan, India. *Ore Geology Reviews*, **151**, Article 105204. https://doi.org/10.1016/j.oregeorev.2022.105204

[45] Warren, I., Simmons, S.F. and Mauk, J.L. (2007) Whole-Rock Geochemical Techniques for Evaluating Hydrothermal Alteration, Mass Changes, and Compositional Gradients Associated with Epithermal Au-Ag Mineralization. *Economic Geology*, **102**, 923-948. https://doi.org/10.2113/gsecongeo.102.5.923

[46] Kaeter, D., Barros, R., Menuge, J.F. and Chew, D.M. (2018) The Magmatic-Hydrothermal Transition in Rare-Element Pegmatites from Southeast Ireland: LA-ICP-MS Chemical Mapping of Muscovite and Columbite-Tantalite. *Geochimica et Cosmochimica Acta*, **240**, 98-130. https://doi.org/10.1016/j.gca.2018.08.024

[47] Xu, L., Chen, L., Zhao, J., Li, J., Wang, S., Li, J., Yang, B., Wang, H. and Lu, W. (2023) Magmatic-Hydrothermal Evolution of the Dangba Rare-Metal Granitic Pegmatites in the Songpan-Ganzê Orogenic Belt, Eastern Tibet: Insights from Muscovite and Columbite-Group Minerals.

[48] Bowden, P., Batchelor, R.A., Chappell, B.W., Didier, J. and Lameyre, J. (1984) Petrological, Geochemical and Source Criteria for the Classification of Granitic Rocks: A Discussion. *Physics of the Earth and Planetary Interiors*, **35**, 1-11. https://doi.org/10.1016/0031-9201(84)90029-3

[49] Valori, A., Teklemariam, M. and Gianelli, G. (1992) Evidence of Temperature Increase of CO_2-Bearing Fluids from Aluto-Langano Geothermal Field (Ethiopia): A Fluid Inclusions Study of Deep Wells LA-3 and La-6. *European Journal of Mineralogy*, **4**, 907-920. https://doi.org/10.1127/ejm/4/5/0907

[50] Idrus, A., Kolb, J. and Meyer, F.M. (2009) Mineralogy, Lithogeochemistry and Ele-

mental Mass Balance of the Hydrothermal Alteration Associated with the Gold - rich Batu Hijau Porphyry Copper Deposit, Sumbawa Island, Indonesia. *Resource Geology*, **59**, 215-230. https://doi.org/10.1111/j.1751-3928.2009.00092.x

[51] Kamar, M.S., Moghazy, N.M. and Saleh, G.M. (2021) Pan-African Rare Metals Bearing Pegmatites in Wadi Ghadir, South Eastern Desert, Egypt: The Geochemical Evolution and Implications for Mineralization. *SN Applied Sciences*, **3**, Article No. 427. https://doi.org/10.1007/s42452-021-04414-w

[52] Li, B., Zhao, L., Lu, A., Luo, J.B., Kong, H. and Lai, J.Q. (2024) Mineralogical Constraints on Pegmatite Genesis and Rare Metal Mineralization in the Mufushan Batholith, South China. *Ore Geology Reviews*, **164**, Article 105856. https://doi.org/10.1016/j.oregeorev.2023.105856

[53] Gmochowska, W., Wirth, R., Słaby, E., Anczkiewicz, R., Krzątała, A., Roddatis, V., *et al.* (2024) Hydrothermal Alteration of Accessory Minerals (Allanite and Titanite) in the Late Archean Closepet Granitoid (Dharwar Craton, India): A TEM Study. *Geochemistry*, **84**, Article 126130. https://doi.org/10.1016/j.chemer.2024.126130

[54] Zhong, F., Wang, L., Wang, K., Liu, J., Zhang, Y., Li, H., *et al.* (2023) Mineralogy and Geochemistry of Hydrothermal Alteration of the Mianhuakeng Uranium Deposit in South China: Implications for Mineralization and Exploration. *Ore Geology Reviews*, **160**, Article 105606. https://doi.org/10.1016/j.oregeorev.2023.105606

[55] Wang, L.X., Ma, C.Q., Lai, Z.X., Marks, M., Zhang, C. and Zhong, Y.F. (2015) Jurassique inférieur mafic dykes from the Xiazhuang ore district (South China): Implications for tectonic evolution and uranium metallogenesis. *Lithos*, **239**, 71-85. https://doi.org/10.1016/j.lithos.2015.10.008

[56] Luo, J.C., Hu, R.Z., Fayek, M., Li, C.S., Bi, X.W., Abdu, Y. and Chen, Y.W. (2015) In-situ SIMS Uraninite U-Pb Dating and Genesis of the Xianshi Granite-Hosted Uranium Deposit, South China. *Ore Geology Reviews*, **65**, 968-978. https://doi.org/10.1016/j.oregeorev.2014.06.016

[57] Zhang, Z.S. (2011) Xiazhuang Uranium Ore Field: Role of Ore-Forming Fluids and Uranium Metallogenesis. China Atomic Energy Press.

[58] Chen, Y.W., Bi, X.W., Hu, R.Z. and Dong, S.H. (2012) Element Geochemistry, Mineralogy, Geochronology and Zircon Hf Isotope of the Luxi and Xiazhuang Granites in Guangdong Province, China: Implications for U Mineralization. *Lithos*, **150**, 119-134. https://doi.org/10.1016/j.lithos.2012.06.025

[59] Bonnetti, C., Liu, X., Mercadier, J., Cuney, M., Wu, B. and Li, G. (2021) Genesis of the Volcanic-Related Be-U-Mo Baiyanghe Deposit, West Junggar (NW China), Constrained by Mineralogical, Trace Element and U-Pb Isotope Signatures of the Primary U Mineralisation. *Ore Geology Reviews*, **128**, Article 103921. https://doi.org/10.1016/j.oregeorev.2020.103921

[60] Ballouard, C., Poujol, M., Boulvais, P., Mercadier, J., Tartèse, R., Venneman, T., *et al.* (2017) Magmatic and Hydrothermal Behavior of Uranium in Syntectonic Leucogranites: The Uranium Mineralization Associated with the Hercynian Guérande Granite (Armorican Massif, France). *Ore Geology Reviews*, **80**, 309-331. https://doi.org/10.1016/j.oregeorev.2016.06.034